Cover Sheet

Title:
Linking silicon isotopic signatures with diatom communities

Authors and Affiliations:

Kerry Schmidtbauer, Department of Geological Sciences and Engineering, University of Nevanda, Reno, NV 89557, USA, kerrylhoward@gmail.com

Paula Noble, Department of Geological Sciences and Engineering, University of Nevanda, Reno, NV 89557, USA and Global Water Center, University of Nevada, Reno, NV 89557, USA, noblepj@unr.edu

Michael Rosen, Global Water Center, University of Nevada, Reno, NV 89557, USA and Department of Geological Sciences and Engineering, University of Nevanda, Reno, NV 89557, USA, mrosen@usgs.gov

Daniel J. Conley, Department of Geology, Lund University, Lund, Sweden, daniel.conley@geol.lu.se, @DrSilica

Patrick J. Frings, Earth Surface Geochemistry, GFZ German Research Centre for Geosciences, Potsdam, Germany, patrick.frings@gfz-potsdam.de, @PatrickJFrings

This paper has been published in *Geochimica et Cosmochimica Acta 323 (2022) 102–122*
https://doi.org/10.1016/j.gca.2022.02.015

1 **Linking silicon isotopic signatures with diatom communities**

2 Kerry Schmidtbauer[1], Paula Noble[1,2], Michael Rosen[2,3], Daniel J. Conley[4], Patrick J.
3 Frings[5]*

4 [1] Department of Geological Sciences and Engineering, University of Nevada, Reno,
5 NV 89557, USA

6 [2] Global Water Center, University of Nevada, Reno, NV 89557, USA

7 [3] United States Geological Survey, Carson City, NV 89701, USA

8 [4] Department of Geology, Lund University, Lund, Sweden

9 [5] Earth Surface Geochemistry, GFZ German Research Centre for Geosciences,
10 Potsdam, Germany

11 *corresponding author: patrick.frings@gfz-potsdam.de

12

13 **Abstract**

14 The use of silicon isotope ratios (expressed as $\delta^{30}Si$) as a paleolimnological
15 proxy in lacustrine systems requires a better understanding of the role of lake processes
16 in setting the $\delta^{30}Si$ values of dissolved Si (dSi) in water and in diatom biogenic silica
17 (bSi). We determined the $\delta^{30}Si$ of modern dSi ($\delta^{30}Si_{dSi}$) and bSi ($\delta^{30}Si_{bSi}$) in three lakes
18 in Lassen Volcanic National Park (LAVO), California (USA), and produced diatom
19 assemblage compositional data from the modern system and from sediment core
20 samples. In the modern systems, we observe the largest magnitude diatom Si isotope
21 fractionations yet reported, at -3.4 and -3.9‰ for *Fragilaria* dominated samples. Using
22 statistical approaches designed to condense multivariate ecological data, we can
23 deconvolve assemblage-specific Si isotope fractionations from the combined diatom
24 assemblage-$\delta^{30}Si$ data. For example, samples dominated by generally deeper water

euplanktic species have low $\delta^{30}Si_{bSi}$ values (< -1.10‰). Conversely, samples dominated by shallow water planktic or benthic periphyton have higher $\delta^{30}Si_{bSi}$ values (> -0.14‰). These data suggest that $\delta^{30}Si$ records from LAVO lakes reflect species specific Si isotope fractionations and thus act as paleolimnological proxy for the aquatic-habitat of bSi production. Silicon isotope analysis should be coupled with diatom community composition data and other geochemical proxies for the most robust paleolimnological interpretations. We also construct a Si mass-balance for Manzanita Lake based on elemental fluxes. Despite a short residence time of ~4 months, it is an efficient Si sink: about 30% of inflowing Si is retained in the lake sediments. An entirely independent Si isotope-based estimate agrees remarkably well. Burial fluxes of bSi derived from radiometrically dated sediment cores yield retention rates of about a factor of three higher, which might suggest groundwater is an important term in the lake Si budget.

1. Introduction

Diatoms, through their prodigious uptake of dissolved Si (dSi) and rapid mineralization of biogenic Si (bSi), are central to freshwater Si cycling. Understanding diatom uptake and recycling of this often limiting nutrient therefore shines light on the continental Si cycle (Frings et al., 2014) and lake phytoplankton ecology (e.g. Kilham, 1971). Silicic acid is delivered to lakes from either surface water or groundwater, and ultimately derives from the weathering of silicate minerals. Within-lake recycling of biogenic silica is also important, as most freshwater systems are strongly undersaturated with respect to bSi, particularly during periods of enhanced biological activity where Si is removed from the water column. Given its role as a key nutrient in lake ecology, and its coupling to the carbon cycle via the silicate-weathering feedback (Frings, 2019), there is considerable incentive to be able to reconstruct aspects of the past Si cycle. As integrators of catchment biogeochemistry, lake sediment archives are ideally placed to achieve this, but estimates of bSi concentrations or accumulation rates can paint an incomplete or misleading picture (Nantke et al., 2021).

Silicon isotope ratios (expressed as $\delta^{30}Si$) are emerging as a powerful tool to trace Si biogeochemistry. Differences in $\delta^{30}Si$ between two phases result from isotope fractionation, that can be expressed as a fractionation factor α, defined as $\alpha_{A\text{-}B} = R_A/R_B$, where R is the ratio $^{30}Si/^{28}Si$ in phase A and B. Since $\alpha_{A\text{-}B}$ is typically very close to unity it can also be presented in ε notation (Coplen, 2011), where $\varepsilon_{A\text{-}B} = \alpha_{A\text{-}B} - 1$ and is typically given in per mille. Si is incorporated in the diatom frustule as bSi (a hydrated, amorphous silicon oxide or $SiO_2 \cdot nH_2O$; De La Rocha et al. 1998). This typically occurs with a discrimination against the heavier isotopes. This leaves the residual dissolved Si enriched in the heavier Si isotopes (i.e. higher $\delta^{30}Si$), while the bSi in the diatom frustule

becomes isotopically lighter (De La Rocha et al., 1997). In other words, $\varepsilon_{A\text{-}B} < 0$ or $\alpha_{A\text{-}B} < 1$ (De La Rocha et al., 1997; Frings et al., 2016; Opfergelt and Delmelle, 2012). Estimates of the fractionation ε associated with the biological uptake of Si by freshwater diatoms, as compiled by (Frings et al., 2016), are around -2.0 to -1.0 ‰

To our knowledge, no laboratory investigations of freshwater taxa Si isotope fractionation have been performed. The limited field-based data that exist include estimates of ε = -1.61 ‰ in Lake Baikal (Panizzo et al., 2016), -1.10 ‰ in Lake Tanganyika (Alleman et al., 2005) and -1.04 ‰ in Icelandic Lake Myvatn (Opfergelt et al., 2011). Sun et al. (2018) interpret a downstream increase in $\delta^{30}Si$ of dSi in the Lena River as reflecting diatom activity, and derive a Si isotope fractionation ε = -1.40 ‰. A similar value was derived for diatoms blooming in the eutrophic Oder River (Sun et al., 2013). While these values are broadly consistent with each other, and with marine taxa, the variability hints at environmental controls, species-specific isotope fractionations, or habitat-specific variability that are not yet fully understood.

Two simple models can be used to predict and interpret the evolution of silicon isotope compositions as a function of the fraction of the available dSi converted to diatom bSi, with an associated isotope fractionation $\varepsilon_{A\text{-}B}$. The first considers the evolution of isotope ratios in a finite pool of dSi that is converted to bSi with no reverse reaction. This is commonly referred to as a "closed" system or Rayleigh model. Under the conditions of this model, as bSi is produced and dSi is consumed, both $\delta^{30}Si_{bSi}$ and $\delta^{30}Si_{dSi}$ evolve towards higher values when ε is negative:

$$\delta^{30}\mathrm{Si_{dSi}} = \delta^{30}\mathrm{Si_{init}} + \varepsilon_{dSi-bSi} \cdot \ln f \quad \text{Eqn. 1a}$$

$$\delta^{30}\mathrm{Si}^{*}_{bSi} = \delta^{30}\mathrm{Si_{dSi}} + \varepsilon \quad \text{Eqn. 1b}$$

$$\delta^{30}\mathrm{Si_{bSi}} = \delta^{30}\mathrm{Si_{init}} - \varepsilon(f \ln f / 1 - f) \quad \text{Eqn. 1c}$$

Where the subscript 'init' denotes the δ^{30}Si of the dSi initially supplied (e.g. of the river flow into a lake), and f is the fraction of initial dSi remaining (i.e. at $f = 1$, no diatom growth has occurred, and at $f \to 0$, all available dSi has been used). $\delta^{30}Si^{*}_{bSi}$ indicates the instantaneously produced bSi, which is always one fractionation offset from the coeval dSi. The cumulative product is given in Eqn. 1c. The alternative model is a steady-state or "open" system where there is a constant supply of new dSi with constant δ^{30}Si into the system, of which a fraction is converted to bSi:

$$\delta^{30}\mathrm{Si_{dSi}} = \delta^{30}\mathrm{Si_{init}} - \varepsilon(1-f) \quad \text{Eqn. 2a}$$

$$\delta^{30}\mathrm{Si_{bSi}} = \delta^{30}\mathrm{Si_{init}} + \varepsilon f \quad \text{Eqn. 2b}$$

Again, both $\delta^{30}\mathrm{Si_{bSi}}$ and $\delta^{30}\mathrm{Si_{dSi}}$ will evolve towards higher values, but along different trajectories than that of the Rayleigh model. In this model, the bSi instantaneously produced and the cumulative product have the same composition. Note that evolution of δ^{30}Si as a function of reaction completeness in a closed system but where both forward and reverse reactions occur at equilibrium has the same mathematical form as the 'steady-state' model. For this reason, we use 'Rayleigh' and 'steady-state' to distinguish between the two models. Two endmember possibilities for the bSi produced are shared by both models. Firstly, at 0% utilization (i.e. $f = 1$) an infinitesimally small amount of diatom Si uptake will produce bSi offset by exactly one fractionation from the source dSi. Secondly, at 100% Si utilization (i.e. $f = 0$) the bSi must have the same δ^{30}Si as the source dSi ($\delta^{30}\mathrm{Si_{init}}$). The models differ in their predictions for intermediate utilizations, but crucially both predict increasing $\delta^{30}\mathrm{Si_{bSi}}$ with increasing dSi utilization. This forms the basis of silicon isotope ratios as a paleoproductivity proxy (De La Rocha et al., 1998). From this simple framework, the source pool dSi isotope composition (i.e. $\delta^{30}\mathrm{Si_{init}}$), and the Si isotope fractionation ε

109 associated with diatom production, emerge as key parameters. If these are constrained,
110 then we are able to quantitatively interpret diatom $\delta^{30}Si$ in terms of Si utilization (i.e.
111 f).

112 There is a growing body of research using Si isotopes as proxies for diatom
113 productivity in freshwater systems (Chen et al., 2012; Swann et al., 2010), or for
114 interpreting environmental change more generally (Cockerton et al., 2015; Nantke et
115 al., 2021; Nantke et al., 2019; Street-Perrott et al., 2008). These depend on a robust
116 understanding of Si cycling in modern settings (Alleman et al., 2005; Panizzo et al.,
117 2017; Sun et al., 2014), though knowledge gaps exist. For example, the range of
118 plausible Si isotope fractionations and the potential for species-specific fractionations
119 ('vital effects') is poorly constrained, though marine studies offer some guidance. The
120 first laboratory study of three marine diatom taxa yielded consistent Si isotope
121 fractionations of -1.1‰ (De La Rocha et al., 1997). Subsequent work broadly
122 corroborated the magnitude of fractionation, but also indicated that marine diatom Si
123 isotope fractionation is more variable. Published estimates for both freshwater and
124 marine diatoms range from -2.09 to -0.54‰ (Sutton et al., 2013). As well as intrinsic
125 differences in Si processing by different taxa, variability in the isotope fractionation,
126 could also plausibly be influenced by environmental conditions including (micro-
127)nutrient availability, temperature, or growth rate. Superimposed on this, diatom habitat
128 in the water column or seasonality of growth can affect the final measured $\delta^{30}Si$ if the
129 source pool $\delta^{30}Si$ is spatially or temporally variable. Whether the system is best
130 described by a steady-state or Rayleigh model further complicates interpretation of the
131 measured ratio (e.g. Closset et al., 2016; Varela et al., 2004).

132 Here, we explore the influence of diatom community composition and lake

characteristics on $\delta^{30}Si_{bSi}$ in three diatom-dominated lakes in Lassen Volcanic National Park (LAVO), California. These wilderness-area aquatic systems are of management concern because they are keystone aquatic resources in LAVO, and as such these lakes are well-studied with respect to other nutrients and anthropogenic impacts. These lake systems also have wider significance, in that they are potential recorders of regional hydroclimate (Howard and Noble, 2018). A diversity of microhabitats and susceptibility of ecosystem functioning to anthropogenic perturbation means that observations here are easily translated to other small lake systems around the world. Here, we present Si isotope data in combination with analysis of diatom community composition and limnological parameters from these three lakes. Our objectives are to investigate links between $\delta^{30}Si_{bSi}$ values and diatom communities in LAVO lakes to better guide interpretations of down-core $\delta^{30}Si_{bSi}$ in lake systems.

2. Study sites

The locations and catchment areas of Manzanita Lake (ML), Butte Lake (BL), and Widow Lake (WL) in LAVO are presented in Figure 1. Lakes in this region tend to polymictic to dimictic (i.e. exhibiting vertical stratification on emphemeral- to seasonal-timescales). The combined catchment area of these three lakes comprises approximately 33% of LAVO, and also includes a small area outside the park boundary.

2.1 Manzanita lake

Manzanita Lake, located in the northwestern corner of the park (Figure 1), is fed by Upper Manzanita Creek with headwaters located on the northwestern flank of Lassen Peak. Manzanita Lake has a maximum depth of 9-10 m and was formed approximately 350 years ago when a series of landslides (Chaos Jumbles) broke off

Chaos Crags and flowed approximately 6 km damming Manzanita Creek (Clynne et al., 2008; Clynne and Muffler, 2010). Upper Manzanita Creek (UMC) drains Chaos Crags lava domes, which were emplaced approximately 1050 years ago (Clynne et al., 2008). The bedrock geology of the ML watershed is dominated by rhyodacite and other easily erodible high-Si extrusive igneous rocks. ML was artificially dammed in 1913, which raised the lake level by ~0.6 m (Clynne et al., 2012). Lower Manzanita Creek (LMC) continues past the dam and serves as the only outlet to ML.

2.2 Butte Lake

Butte Lake, in the northeastern region of the park (Figure 1), is situated amidst the Fantastic Lava Beds near the Cinder Cone. This area of the park is dominated by extrusive igneous rocks of andesitic composition. Butte Lake is a remnant of a larger lake that was partly filled by lava flows during the eruption of the Cinder Cone approximately 350 years ago (A.D. 1666) (Clynne et al., 2000). The maximum depth of the lake is 13-15 m, and the lake is thermally stratified during summer months (Howard and Noble, 2018). Butte Lake is mainly supplied by water seeping beneath the Fantastic Lava Beds from Snag Lake, which was formed when the Painted Dunes lava flow (Cinder Cone) blocked Grassy Creek, a stream draining the central highland of LAVO (Clynne et al., 2000). Ephemeral surface outflow from BL is into Butte Creek and is directly related to inter-annual fluctuations in precipitation and snowpack. Butte Lake is hydrologically interesting site because it oscillates between being a hydrologically open and closed system for surface water flows (Howard and Noble, 2018), depending on the degree of winter precipitation.

2.3 Widow Lake

Widow Lake is located in the northeastern region of the park, approximately 2 km from the southeastern margin of BL (Figure 1) and sits on a volcanic highland beyond a ridge about 234 m above BL. Widow Lake lies within the Butte Lake watershed, occupying about 4% of BL catchment. The bedrock geology is dominated by extrusive igneous rocks of basaltic-andesitic composition. The maximum lake depth of WL is 9-10 m, and because no permanent surface water inflow landforms are present, the lake is likely supported mainly by groundwater and surface runoff from snow melt in the spring. Widow Lake is surrounded by locally derived glacial sediments (Clynne and Muffler, 2010) and is therefore likely a post-glacial lake, formed in a topographic low or in a kettle hole (a pit formed by a detached ice block during glacial retreat).

3. Materials and Methods

3.1 Field sampling and initial sample preparation

Physical and chemical characteristics (described below) were measured, and water/phytoplankton samples were taken around the same time of day (early afternoon) and in the same location in ML and WL during monthly sampling trips in the summer months of 2012, 2013, and 2014, giving sequential snapshots of lake structure. Sediment samples for diatom community composition, bSi concentrations, and silicon isotope analyses were taken from three (<1m) continuous lake-sediment cores with an intact sediment-water interface that were collected in 2012 (WL), 2013 (ML), and 2014 (BL). The WL core was taken using a Multi-Use Coring Kit (MUCK) gravity coring device, and the ML and BL cores were taken using a Livingstone type push-coring device (Glew et al., 2001).

3.1.1 Physical measurements

Surveys to determine maximum depth (m) and identify sampling locations for each lake were performed using a sonar depth finder. Thermal and chemical profiles (temperature, dissolved oxygen, conductivity) were measured at each sampling location with a YSI-85 multiparameter instrument (Xylem Incorporated) that was calibrated in the lab before being taken to the field on each sampling date. Thermal and chemical profiles were then used as a determinant of lake structure and to define the locations of the epi-, meta-, and hypo- limnia at each sampling location. Water clarity was measured using a Secchi disk. Discharge was estimated at a location above ML in UMC and at a location in LMC below ML using Manning's equation and the slope-area method of discharge estimation (Dalrymple and Benson, 1968; Online Supplementary Material). These estimates were then coupled with an estimate of lake volume to calculate a range of hydraulic residence times for ML, where the hydraulic residence time (HRT) is defined as the time required to fill an empty lake with its natural inflow and can be calculated by dividing lake volume by inflow or outflow rate. Mean and median discharges calculated from discharges measured in LMC from August 1979-September 1981 at a USGS stream gauge (site #11376038) were also used to estimate an average HRT for ML. Various catchment and lake characteristics were also determined, including lake volume, surface area, drainage ratio, curve number (a measure of surface runoff potential) following methods described in (Howard and Noble, 2018).

3.1.2 Chemical and phytoplankton samples

Water and phytoplankton samples from ML, UMC, LMC, BL, and WL were collected in the spring, summer, and fall of 2014 for silicon isotope analyses, chlorophyll-*a* (Chl-*a*) and diatom analyses. Water was sampled using a Van Dorn sampler at several predetermined depths to capture of snapshot values from the epi-,

meta-, and hypolimnion of each lake, and from the surface (0 m) in UMC and LMC. (Epilimnion, metalimnion and hypolimion refer to the upper, intermediate and lower thermal layers in a stratified lake). Samples for $\delta^{30}Si$ analysis of ca. 100 ml were filtered in the field through 0.4 μm polycarbonate (PC) filters (Whatman-Nuclepore) and stored in acid-cleaned, opaque, polyphenylene ether (PPE) plastic bottles and kept cool in the dark until return from LAVO. Chl-*a* and pheophytin were measured from 100 mL of water via fluorometry (Turner Designs model 10AU Fluorometer) using methanol as a solvent to determine algal biomass (Welschmeyer, 1994). Calibration was conducted using a spectrophotometric method (Parsons et al., 1984) and a standard, Chl-*a* from *Anacystis nidulans* (Sigma Corp.). Samples of lake diatoms for identification, enumeration, and silicon isotope analysis were taken from: 1) surface tows (~300 m) using a 20 μm plankton net; and 2) from substrate scrapes at the lake margin, and 3) near surface inflow and outflow (ML only). The plankton tow and substrate scrape samples were stored in acid-cleaned PPE bottles and kept on ice and then refrigerated before sample preparation.

3.1.3 Sediment core samples

Lake cores were stabilized with Zorbitrol (sodium polyacrylate absorbent powder) upon recovery in the field and then refrigerated before being sent to the National Lacustrine Core facility (LacCore) in Minnesota, USA. At LacCore, the cores were split and subsampled at a 0.5 cm or 1 cm resolution. Sediment samples from the cores were freeze-dried and stored in opaque polyethylene containers before further sample preparation and analysis. Age-depth models of the BL, ML, and WL cores were established by ^{210}Pb and ^{137}Cs dating at Flett Research Ltd (Canada), using a gamma spectroscopy technique for ^{137}Cs and an alpha spectrometry method modified from

(Eakins and Morrison, 1978) for ^{210}Pb. Radioisotope data from BL and ML were analyzed using the slope-regression and constant rate of supply (CRS) models (Appleby, 2001; Appleby and Oldfield, 1978; Pourchet et al., 1989). Radioisotope data for WL were analyzed using a linear slope-regression model (Appleby, 2001; Appleby and Oldfield, 1978; Pourchet et al., 1989). A CRS model could not be applied to WL ^{210}Pb data, because bulk density was not measured during core sampling. Analysis for percent bSi was conducted at the Sedimentary Records of Environmental Change Laboratory (Northern Arizona University) using a wet-alkaline method of extraction (Mortlock and Froelich, 1989). Briefly, ~20 mg of crushed freeze-dried sediment is leached for 5 hr in 40 ml of 2M Na_2CO_3, then neutralized and analyzed for dissolved Si concentration spectrophotometrically.

3.2 Diatom enumeration

Prior to cleaning, "boil-and-burn" mount slides were made from all samples to examine the algal communities, including colony formation. Preparation of modern and sediment samples for diatom enumeration followed protocols described in Battarbee et al. (2001) and Stoermer et al. (1995). Diatom community enumeration was carried out on samples also analyzed for $\delta^{30}Si_{bSi}$, including modern plankton, periphyton, and sediment. Permanent slide mounts were made using ZRAX and were used to determine relative abundance counts (n = 500). Samples were also examined during counting for presence of chrysophytes and sponge spicules and presence was recorded in count data. They were rare in all cleaned samples (<1% of counts) and are not discussed further. Diatoms were identified and counted at 1000x using an oil immersion lens with DIC (differential interference contrast) on an Olympus BX51 microscope.

3.3 Si isotope preparation and analysis

Following the method described by De La Rocha et al. (1996), a solution of acidified Triethylamine molybdate (TEA-Moly) was added to the lake water samples and dSi was precipitated overnight. This protocol aims to purify Si from all components of the sample matrix (cationic, anionic, organic). The precipitate (triethylamine silicomolybdate) in each sample was collected by vacuum filtration onto a 0.2 µm polycarbonate filter and placed into a platinum crucible. The crucibles were placed into a muffle furnace and sequentially combusted at 350 °C for 30 minutes to remove residual water, 500 °C for 2 hours to remove organics; and 1000 °C for 10 hours to volatilize the molybdenum. The relatively pure silica (SiO_2) left in each crucible was weighted and then dissolved in an excess of 40% HF. A molar Si:F ratio of 1:100 was targeted to avoid the formation of volatile SiF_4, and diluted to a target Si concentration of 229.9 mM. Any loss of Si during the processing is physical, i.e. without the potential for isotope fractionation. Next, following the anion exchange protocol outlined in Engström et al. (2005), samples were loaded onto anion exchange columns filled with 1.5 ml AG 1-X8 resin (100–200 mesh; Eichrom). Matrix elements were eluted with 95 mM HCL and 22.6 mM HF, and Si was eluted with a solution of 0.15 M HNO_3 and 5.5 mM HF. Complete recovery was verified by colourimetric determination of dSi concentrations in the elutant after complexing the fluoride ions with boric acid. Matrix matched standards were used for the colourimetry.

Diatom surface tow samples, substrate scrape samples, and selected sediment samples from cores were processed using techniques described in Morley et al. (2004). First, several grams of bulk sediment and substrate scrape sample (several milliliters for each surface tow sample) were cleaned with H_2O_2 and HCl to remove organic matter

297 and any trace carbonates. The bSi was then separated from other detrital material in the
298 samples by heavy liquid separation using sodium polytungstate (SPT) at a density of
299 ca. 2.26 g cm^{-3}. The resulting bSi material was inspected under SEM for any
300 contamination (e.g. mineral material); no obvious contamination was observed in
301 checks of modern or sediment samples. Coupled with the negligble presence of non-
302 diatom biosilcifiers (see below) observed in relative abundance counts under light
303 microscopy demonstrates that the $\delta^{30}Si_{bSi}$ data generated reflects diatom biomass. As
304 reported above for water samples, the resulting cleaned and separated bSi fractions
305 were then dissolved in an excess of HF and processed via anion exchange
306 chromatography as above.

307 Silicon isotope ratios of the samples were measured on a Neptune (Thermo
308 Scientific) multi-collector inductively coupled plasma mass spectrometer (MC-
309 ICPMS) at the Pole Spectrométrie Océan (PSO, Ifremer, Brest). The Neptune was
310 operating in medium-resolution mode with a mass-resolution (m/Δm) of > 3500 at 5
311 and 95% peak height. All solutions were doped with a matching Mg concentration and
312 the $^{24}Mg/^{26}Mg$ ratio was monitored dynamically in order to monitor and correct the Si
313 isotope ratios for instrumental mass-fractionation, assuming an exponential
314 fractionation law (Cardinal et al., 2003). The corrected ratios are then used to calculate
315 the $\delta^{30}Si$ and $\delta^{29}Si$ values, i.e. the deviation in the $^{30}Si/^{28}Si$ or $^{29}Si/^{28}Si$ ratios in per mil
316 from bracketing analyses of the NBS28 standard, a reference material of quartz grains
317 distributed by the National Institute of Standards (NIST):

318
$$\delta^{30}\mathrm{Si} = \left(\frac{{}^{x}\mathrm{Si}/{}^{28}\mathrm{Si}_{\mathrm{SMP}}}{{}^{x}\mathrm{Si}/{}^{28}\mathrm{Si}_{\mathrm{NBS28}}} - 1 \right) \qquad \text{Eqn. 3}$$

319 where ${}^{x}\mathrm{Si}/{}^{28}\mathrm{Si}$ are the Mg-corrected isotope ratios of the sample and the

320 average of the bracketing NBS28 standards, with x = 29 or 30. Secondary reference
321 materials (Diatomite, and Big-Batch) were prepared as described above and measured
322 in the same analytical sessions. The results (Big Batch = -10.35±0.31; Diatomite =
323 1.20±0.06) were in good agreement with previously published values (Oelze et al.,
324 2016; Reynolds et al., 2007). The mean absolute deviation between full procedural
325 replicates (n = 15) was 0.08±0.05‰. A three-isotope plot of all samples (Figure 2)
326 defines the relationship $\delta^{30}Si = 1.93.\delta^{29}Si$ ($r^2 = 0.99$, n = 77), equivalent to an expected
327 kinetic or equilibrium mass-dependent fractionation line, and confirming the successful
328 removal of potential polyatomic interferences during preparation and measurement.

329 ***3.4 Diatom numerical analyses***

330 Non-metric multidimensional scaling (NMDS) was conducted on the diatom
331 count data set for all modern and sediment core samples (PC-Ord 6, Autopilot mode,
332 Sorenson distance measure, 250 iterations (McCune and Grace, 2002)). NMDS is an
333 ordination technique well-suited to count-data that condenses multivariate datasets (e.g.
334 diatom count data) to a small number of Cartesian axes in such a way that distance
335 between samples is maintained. $\delta^{30}Si_{bSi}$ values were plotted as an environmental
336 variable overlay vector on the NMDS ordination.

337 Samples were subjected to constrained clustering using $\delta^{30}Si_{bSi}$ values from
338 modern and down-core samples using the Rioja R package (Juggins and Juggins, 2020;
339 https://github.com/nsj3/rioja). An optimal number of clusters was determined using a
340 Mantel (Pearson) method of correlation between the original distance matrix and binary
341 matrices computed from the dendrogram cut at various levels (Borcard et al., 2018).
342 Indicator species analysis was conducted on each cluster group (PC-Ord 6, Dufrêne and

Legendre (1997) method, 4999 permutations in the Monte Carlo test). Finally, a multi-response permutation procedure (MRPP) was conducted as a significance test for differences between/within the cluster groups based on within-group diatom taxa similarities (PC-Ord 6, Sorenson distance measure; Peck (2016)). The output of MRPP includes the test statistic T, which indicates separation among groups, and an effect size A, that refers to the chance-corrected, within-group agreement. When A = 1 there is homogeneity within groups and when A = 0 there is heterogeneity within groups (McCune and Grace, 2002). P-values are produced using permutation, and indicate how likely an observed difference between groups is as a result of chance (McCune and Grace, 2002). A ≤ 0.4 is considered a 'large' effect size (Peck, 2016), though this may change as our understanding of this novel statistic improves (Peck, 2016).

4. Results

4.1 Lake characteristics

A summary of catchment characteristics and lake physicochemical parameters are reported in Table 1 for ML, WL, and BL. An in-depth discussion of catchment characteristics, lake physicochemical parameters, modern diatom community succession, and Chl-*a* values for Butte Lake (BL) is presented in Howard and Noble (2018). Table 2 presents the modern water samples and phytoplankton silicon isotope compositions and Chl-*a* concentrations (a proxy for phytoplankton biomass). All lake characteristic data (e.g. oxygen, chlorophyll, temperature, conductivity) are given in the online supplementary data file. Diatom relative abundance counts, sediment core bSi contents and sediment $\delta^{30}Si_{bSi}$ values are given in the online Supplementary Data. Diatoms dominate the phytoplankton samples from all lakes, though BL and WL have

366 higher mean Chl-*a* values than ML (Table 2). Both ML and WL appear to have a
367 subsurface Chl-*a* maximum in the summer. As with BL (Howard and Noble, 2018),
368 ML and WL have a consistent, planktic diatom succession following ice-out in the
369 spring, through to the fall, although the community composition differs between the
370 lakes.

371 *4.1.1 Manzanita lake*

372 Vertical profiles of temperature, conductivity, and dissolved oxygen across
373 three years of monitoring are shown in Figure 3A. In ML, the seasonal progression of
374 stratification was similar during each year of the monitoring period as was the mixing
375 depth (~3-4 m) during stratification. The vertical profiles reflect a stratified structure,
376 where hypolimnetic temperatures increased through the period of stratification.
377 Estimated average hydraulic retention time for ML is ~4 months. Manzanita Lake is
378 distinguished hydrologically from either BL or WL by the influence of Manzanita
379 Creek, with surface water inflows and outflows observed over the algal growing
380 seasons in 2012-2014.

381 The $\delta^{30}Si_{dSi}$ values for ML, and ML's inflow and outflows at upper and lower
382 Manzanita Creek, respectively, are reported in Table 2 and plotted in Figure 4. Inflow
383 $\delta^{30}Si_{dSi}$ values in Upper Manzanita Creek are lower than ML or LMC (outflow) $\delta^{30}Si_{dSi}$
384 values. ML $\delta^{30}Si_{dSi}$ values are variable in the epilimnion over the growing season, with
385 the highest value was observed in September 2014 (+2.79 ‰). ML $\delta^{30}Si_{dSi}$ values of
386 the meta- and hypo-limnia in 2014 are similar and near to the baseline level of UMC
387 inflow (+1.01‰) (Figure 4). In ML, $\delta^{30}Si_{bSi}$ varies seasonally, and between
388 phytoplankton and periphyton (Table 3; Figure 5). In general, periphyton diatom $\delta^{30}Si$
389 values were higher than plankton diatom $\delta^{30}Si$ values (Table 3). In ML, Chl-*a* values

suggest that the greatest productivity occurs in the meta- and hypo-limnia with the exception of September 2014, when the highest productivity occurred in epilimnion (Table 2).

In ML, *Asterionella formosa* is abundant in May and June, transitions to *Fragilaria crotonensis* dominance in August, and finally to a mixed *F. crotonensis* and *Aulacoseira granulata* var. *angustissima* assemblage in the fall. The UMC periphyton spring and fall communities differ slightly. There is a greater relative abundance of araphids such as *Diatoma anceps*, *Diatoma mesodon*, *Fragilaria vaucheriae* as well as *Gomphonema* spp in June 2014, whereas the fall community was dominated by monoraphids *Achnanthidium minutissimum* and *Planothidium lanceolatum* and *Nitzschia* spp. (i.e., *Nitzschia dissipata*).

4.1.2 Butte Lake

BL limnological characteristics were reported previously (Howard and Noble, 2018) and outlined in section 2.2. Briefly, the lake undergoes summer stratification following ice-out, persisting into the early fall, with a mixing depth of 5-6 m. Surface dSi concentrations ranged from 2.4 to 3.6 mg/L. Concentrations at 6m depth ranged from 2.6-4.5 mg/L and increased throughout the seasonal succession (Table 2). Epilimnetic $\delta^{30}Si_{dSi}$ values in BL are generally lower than ML and range from +1.30 ‰ (fall) to +1.60 ‰ (summer) (Table 3; Figure 4). The summer hypolimnetic silicon isotope composition of dSi in BL is also enriched in ^{30}Si, with $\delta^{30}Si$ similar to that of the epilimnion (+1.6 ‰), while the other $\delta^{30}Si_{dSi}$ values from the meta- and hypo-limnia are broadly unfractionated relative to inputs, assuming that surface water inflow value of UMC (+1.01‰) is representative of the total Si influx.

Planktic diatom $\delta^{30}Si_{bSi}$ values in BL hint at seasonality with a ~0.13 ‰

414 difference between spring and summer 2014. Spring 2014 had a $\delta^{30}Si_{bSi}$ value of -0.74
415 ‰ during the time it was dominated by the species *F. crotonensis* (Howard and Noble,
416 2018). In summer 2014 $\delta^{30}Si_{bSi}$ was -0.9‰, with the assemblage dominated by
417 *Staurosira construens* var. *binodis* (Howard and Noble, 2018). In addition to species
418 differences, total diatom productivity differed between seasons; total planktic diatom
419 biovolume decreased by ~50% between spring and summer 2014 (Howard and Noble,
420 2018).

421 *4.1.3 Widow Lake*

422 In contrast to ML and BL, the smaller WL does not exhibit sustained
423 stratification, and was nearly isothermal at all sampling dates with the exception of June
424 2012 (Figure 3B). Vertical profiles of conductivity and DO also suggest that WL is a
425 polymictic system where frequent mixing is interspersed with short-term stratification.
426 dSi concentrations are relatively consistent across the sampling period, at 2.4 to 3 mg/L.
427 With a mean of 1.25‰, WL has the lowest epilimnetic $\delta^{30}Si_{dSi}$ values of the three lakes
428 (Table 3). Widow Lake has a different diatom succession than its neighboring lakes;
429 *Tabellaria flocculosa* and *Fragilaria tenera-nanana* group dominate in spring,
430 followed by *F. crotonensis* and *T. flocculosa* in the summer, and *F. tenera-nanana*
431 group in the fall.

432 ***4.2 LAVO lake sediment cores***

433 *4.2.1 Manzanita Lake*

434 Down-core $\delta^{30}Si_{bSi}$ values, percent bSi, and diatom data are shown in Figure
435 5A. Around 1942 CE (Common Era), percent bSi is relatively low (<10%) and a
436 relatively high $\delta^{30}Sib_{Si}$ value (-0.60‰) is observed (Figure 5A). Percent bSi increases

437 and $\delta^{30}Si_{bSi}$ decreases slightly until ~1968 CE. The diatom community composition
438 during this same period is dominated by benthic periphyton (*Navicula* and *Nitzschia*
439 spp), epilithic periphyton (i.e., *Fragilaria vaucheriae*), and meroplankton taxa
440 (*Aulacoseira* spp). From ~1968 CE until 1986 CE, the relative abundances of
441 tychoplankton (i.e., *Staurosira construens var. venter*) and euplanktic taxa
442 (*Stephanodiscus* spp., *F. crotonensis, F. mesolepta*) begin to increase. A simultaneous
443 increase in percent bSi (up to ~20%) and decrease in $\delta^{30}Si_{bSi}$ values (to around -1.0 ‰)
444 is also observed. From 1986 CE to 1998 CE, there is a slight decrease in percent bSi
445 coincident with an increase in $\delta^{30}Si_{bSi}$ values (up to around -0.70 ‰). Relative
446 abundances of euplanktic taxa decrease slightly while relative abundances of
447 tychoplankton (i.e., *Pseudostaurosira brevistriata*, *Staurosira construens* var. *binodis*),
448 meroplankton (i.e., *Aulacoseira granulata* var. *angustissima*) and periphyton taxa (i.e.,
449 *Pseudostaurosira pseudoconstruens*, *Navicula* spp) increase slightly over this period.
450 From 1998 CE to the present, the relative abundances of euplanktic (*F. crotonensis*, *F.*
451 *mesolepta*, *A. formosa*) and tychoplanktic taxa (*S. construens* var. *venter*, *S. construens*
452 var. *binodis*) increase dramatically, concurrently with increases in percent bSi (up to
453 ~30%) and constant $\delta^{30}Si_{bSi}$ values around -0.90 ‰.

454 *4.2.2 Butte Lake sediment core*

455 In the BL core (Figure 5B), prior to the dated section, $\delta^{30}Si_{bSi}$ values are around
456 -0.2 ‰, and decrease upwards to values of -0.9 ‰, tracking consistently with increasing
457 (up to ~70 %) and then decreasing (to ~50%) percent bSi. Decreasing values prior to
458 1932 CE are coincident with increasing relative abundances of euplanktic taxa
459 (*Asterionella formosa, Fragilaria crotonensis, Fragilaria grunowii*). In the dated

section, from ~1932 CE to 2014 CE, there is no correlation between $\delta^{30}Si_{bSi}$ values and percent bSi values is observed: percent bSi remains relatively consistent during this period (at ~50%), while $\delta^{30}Si_{bSi}$ values fluctuate about a trend towards increasing values (around -0.3‰). A major change in diatom community composition occurs in the period from 1932 CE to present, with a decline in the relative abundance of euplanktic taxa and an increase in the relative abundance of small araphid tychoplanktic taxa (i.e., *Staurosira construens var. binodis*).

4.2.3 Widow lake sediment core

WL sediment $\delta^{30}Si_{bSi}$ values vary from -0.5 ‰ to about -0.1 ‰ (Fig 5C). Distinct trends are apparent both below and above the tephra layer (Figure 5C). The highest percent bSi concentrations occur below the tephra layer (beyond the age model), and are correlated with high $\delta^{30}Si_{bSi}$ values. This period is associated with benthic periphyton taxa (i.e., *Sellaphora pupula*, *Pinnularia* spp., *Stauroneis* spp.) and *Discostella stelligera*. Above the tephra layer (~1881 CE to present), the direction of relationship between percent bSi and $\delta^{30}Si_{bSi}$ values change, with higher percent bSi coincident with lower $\delta^{30}Si_{bSi}$ values. This change is also coincident with a change in diatom community composition where euplanktic taxa (i.e., *Fragilaria crotonensis*, *Tabellaria flocculosa*), and tychoplanktic taxa (i.e., *Pseudostaurosira brevistriata*) become dominant. A slight decrease in percent bSi with coincident higher $\delta^{30}Si_{bSi}$ values is noted around 1946 CE and is consistent with an increased relative abundance of *Nitzschia perminuta*, *Achnanthidium minutissimum*, and *Lindavia* spp. Sediment $\delta^{30}Si_{bSi}$ values correlate with percent bSi and phosphorus below the tephra layer in zones 2 and 3, but deviate in zone 1 (Figure 5C), where values become anticorrelated

483 with total P and percent bSi. Similar temporal patterns for $\delta^{30}Si_{bSi}$ values are also
484 observed in BL.

485 ***4.3 Numerical analyses***

486 A δ^{30}Si-constrained cluster analysis yielded six statistically significant sample
487 groups, based on Mantel (Pearson) correlation. One of the groups had only one sample
488 so a total of five groups was chosen for the final analysis. NMDS analysis resulted in a
489 stable solution and stress = 9.44. Axis 1 explains 43% of the variance, Axis 2 explains
490 25% of the variance and Axis 3 explains 18% of the variance. Values of δ^{30}Si correlate
491 best with axis 3 ($r = 0.593$) and axis 1 ($r = 0.339$). Figure 6 shows an NMDS ordination
492 biplot (axes 1 and 3) of all lake core and modern samples with convex hulls delineating
493 the δ^{30}Si-constrained cluster groups and the overlay vector for $\delta^{30}Si_{bSi}$. MRPP among
494 all $\delta^{30}Si_{bSi}$ groups is significant ($p < 0.001$; $\alpha = 0.05$), with a within-group homogeneity
495 effect size of A = 0.26 (Supplementary Material). Significant MRPP p-values and
496 associated A-values (Supplementary Material) indicate that the grouping structure (i.e.
497 clusters produced by the NMDS analysis, constrained by $\delta^{30}Si_{bSi}$) explains a portion of
498 the variation in the response (diatom taxa) distribution and is corroborated by δ^{30}Si
499 values correlating with Axes 1 and 3 in the NMDS ordination (section 4.3) and specific,
500 significant indicator taxa (Table 3). Most pairwise comparisons between the groups are
501 also significant (adjusted P; Holm-Bonferroni correction) at the $\alpha = 0.05$ level
502 (Supplementary Material). Associated significant ($\alpha = 0.05$) indicator taxa were
503 identified for 4 of these 5 groups (Group 2 did not yield any significant indicator taxa
504 at the $\alpha = 0.05$ level) and are given in Table 3.
505 .

5. Discussion

5.1 Patterns of Si utilization in LAVO lakes

Relatively high dSi concentrations (~16 mg/L Si at the UMC inflow, and ~12 mg/L at the LMC outflow; Table 3) compared to the other lakes likely reflect a large drainage ratio, large capacity for surface water runoff (curve number = 63), and the dominant rhyodacite bedrock (Table 1). Beyond these factors, the high dSi concentrations hint at hydrothermal processes seen in the catchment, as reported in general for the LAVO park (Ingebritsen et al., 2016). These values agree well with historical USGS monitoring data for LMC collected in 1979-1981 (mean outflow = 14.8 mg/L Si, no correlation with discharge, USGS site 11376038).

In ML, lower concentrations of dSi in the epilimnion relative to the inflow (~12 mg/L vs. ~17 mg/L, respectively), and higher $\delta^{30}Si_{dSi}$ values (~2.20 ‰ vs. ~1.00 ‰, respectively) suggest utilization of Si throughout the growing season (Table 2, Figure 4). The pattern of higher lake water than inflow water values is consistent amongst all lake studies to date (Alleman et al., 2005; Opfergelt et al., 2011; Panizzo et al., 2017; Zahajská et al., 2021), and is a clear indicator of biological Si uptake. Outflow $\delta^{30}Si_{dSi}$ values in LMC are around +1.86 ‰ (Table 3), lower than epilimnetic values and likely reflect mixing of dSi pools from the metalimnion, hypolimnion, or groundwater into outflow water. High epilimnion $\delta^{30}Si$ suggests most biosiliceous production occurs in the upper water column. Chl-*a* values are a general measure of productivity for all algae groups, and in ML are higher in the meta- and hypolimnia compared to the surface (Table 2). Higher Chl-*a* at depth in ML may result from non-diatom algal groups (e.g., chlorophytes or cyanophytes). Alternatively, the values might reflect export or migration of surface diatom production from the epilimnion to deeper depths. The

530 $\delta^{30}Si_{dSi}$ values of the deeper water samples in ML are lower than the epilimnion either
531 because of lower diatom productivity at depth, the progressive dissolution of diatoms
532 exported from overlying layers or mixing with less ^{30}Si enriched dSi pools (i.e.,
533 groundwater or a diffusive flux across the sediment-water interface).

534 In BL dSi concentrations and $\delta^{30}Si_{dSi}$ values also suggest Si utilization in the
535 epilimnion under stratified conditions (Table 3; Figure 4), with surface waters being ca.
536 0.3 ‰ heavier than deeper waters in May and August 2014. In September 2014, surface
537 water $\delta^{30}Si_{dSi}$ in BL decreased to 1.27‰. indistinguishable to the hypolimnetic value,
538 which we attribute to rigorous vertical mixing after a breakdown in stratification
539 towards the end of the summer season due to decreased air temperatures and storms
540 (see Figure 4 in Howard and Noble (2018)).

541 Unlike ML and BL, WL appears to be continuously mixed and only develops
542 weak stratification on the scale of days (Figure 3). WL only has ephemeral surface
543 water inflow and outflow and has overall lower dSi concentrations (lowest observed
544 was 2.4 mg/L; Table 2), which may reflect a lower weighted curve number for the
545 catchment, smaller drainage ratio, and dominant catchment geology perhaps with a
546 differently reactive suite of minerals than the rhyodacite and andesite underlying ML
547 and BL catchments (Table 1). Chl-*a* values in WL differ between top and bottom under
548 stratified conditions (Table 2) suggesting higher diatom productivity and Si utilization
549 at depth than in the surface water. The one date during which WL exhibited strong
550 stratification, June 21, 2012, shows the greatest variation in epilimnetic (1.29 μg/l) vs
551 hypolimnetic (13.33 μg/l) Chl-*a* values (Table 2). Other sampling dates exhibit much
552 higher Chl-*a* values from surface waters (Table 2) indicating frequent mingling of
553 surface and deeper water in this polymictic system. Unfortunately, dSi concentration

554 and $\delta^{30}Si_{dSi}$ data were not collected for multiple depths in WL so we cannot verify
555 whether increased productivity at depth in WL is linked to enriched $\delta^{30}Si_{dSi}$. Epilimnetic
556 $\delta^{30}Si_{dSi}$ values and dSi concentrations vary slightly over the growing season in WL,
557 suggesting changes in dSi utilization and very weak or short-term stratification (Table
558 3, Figure 3B).

559 *5.1.1 Distinguishing between fractionation models*

560 By plotting $\delta^{30}Si_{dSi}$ and $\delta^{30}Si_{bSi}$ as a function of Si utilized for ML, we can
561 attempt to distinguish between the two endmember fractionation models (see
562 introduction; Figure 7). The x-axis in this plot, i.e. the degree of dSi utilization, is hard
563 to constrain. We take $f = 1 - C/C_0$ as an approximation, where C_0 is the Si
564 concentration of inflows to ML via UMC at the time of sampling and C is the Si
565 concentration of the epilimnion in ML. Accurately accounting for groundwater is not
566 possible, since no wells exist within the park (water supply for consumption is surface
567 water sourced), so we assume the groundwater has the same dSi concentration as UMC.
568 The groundwater dSi should be measured in future work. UMC is thus used as the
569 closest proxy available for background Si concentration of inflows in the absence of
570 biological Si isotope fractionation. Figure 7 shows that the overall range of Si utilization
571 (ca. 19 – 35%; see also section 5.4 below) is not large enough to be able to distinguish
572 Rayleigh-style system evolution (Eqn. 1) from a steady-state model (Eqn. 2). The
573 reality likely falls somewhere between these two endmember scenarios; for much of
574 the growing season, diatom growth rates exceed dSi supply, causing a transient
575 depletion in lake water Si inventory. This lack of balance between supply and removal
576 invalidates the steady-state assumption of Eqn. 2. On the other hand, the non-zero
577 supply of new or recycled dSi, invalidates the assumptions inherent in a Rayleigh

model. Where a system behavior falls between these two models will depend on the rate of bSi production relative to supply; when it is much greater, a Rayleigh model (Eqn. 1) will be closer to the truth, but when they are more closely matched, a Steady-State model (Eqn. 2) may best capture the dynamics of the system. Overall, even simple lake ecosystems cannot be condensed to the models typically used. Seasonal imbalances between supply and demand, combined with variable Si isotope fractionation factors (Section 5.2 below), suggest more nuanced models that capture time-dependence, are required if we are to fully describe system behavior.

5.2 Diatom silicon isotope fractionations

Diatom Si isotope fractionation factors, degree of Si utilization, and degree of system openness combine to define $\delta^{30}Si_{bSi}$ and residual dSi $\delta^{30}Si$ (Section 2). From our LAVO data, we can get a snapshot of the magnitude of the isotope fractionation for diatoms by comparing $\delta^{30}Si_{dSi}$ values with $\delta^{30}Si_{bSi}$ values for diatom samples collected simultaneously, i.e. $\varepsilon_{diatom} \approx \Delta^{30}Si_{water\text{-}diatom} = \delta^{30}Si_{water} - \delta^{30}Si_{diatom}$. Using this approach, we can calculate a Si isotope fractionation for ML planktic diatoms in spring 2014 of -3.4‰ (dominated by *A. formosa* and *F. crotonensis*) and -3.9‰ in fall of 2014 (*F. crotonensis* and *A. granulata* var *anugustissima* dominant) (Figure 7). We can also derive fractionations for BL from 2 paired samplings; in spring of 2014 (-2.29‰, dominated by *F. crotonensis*), summer of 2014 (-2.51 ‰, dominated by *S. construens* var. *binodis*), and for WL in summer of 2014 (-1.58‰, dominated by *F. crotonensis* and *T. flocculosa*). Finally, we can estimate Si isotope fractionations associated with the periphyton taxa growing on ML inflow and outflows (Table 2). This yields a mean value of -1.63 ‰ for three samples. This is an imperfect approach: calculated

601 fractionations may include bias introduced by a mismatch in the timeframe the two
602 pools represent. Dissolved Si δ^{30}Si is effectively an instantaneous value, but diatom bSi
603 δ^{30}Si will integrate over a few lifespans, i.e. days to 10s of days . In general, the
604 estimates for BL and ML fall outside the range of marine diatom taxa Si isotope
605 fractionations presented by Sutton et al. (2013) of -2.09 to -0.53‰, but within the range
606 of Si isotope fractionation observed for marine sponges of ca. -6.75 to – 0.50‰
607 (Cassarino et al., 2018; Hendry and Robinson, 2012). This is an interesting result that
608 warrants deeper investigation.

609 It is well established that marine sponges have variable Si isotope fractionations
610 that exhibit a relationship with the dSi concentrations of the water they grow in (Hendry
611 and Robinson, 2012; Wille et al., 2010). This is thought to be caused by the variable
612 expression of isotope fractionation at different stages of sponge biomineralization
613 (uptake, polymerization, and efflux), in a manner that is governed by mass-balance (cf.
614 Eqn. 2). The presence of various transport proteins is also believed to play a role.
615 Previously, Milligan et al. (2004) have argued that the only fractionating step in diatom
616 biosilicification is the uptake of dSi into the cell. This might suggest that the
617 relationship between ambient dSi concentrations and isotope fractionation seen for
618 sponges would not hold for diatoms. Nevertheless, in compiled marine data, there is a
619 subtle hint of a trend towards larger magnitude Si isotope fractionations at higher dSi
620 concentrations (see Figure 2B in Abelmann et al. (2015)), albeit for ocean surface
621 waters < ~2.2 mg/L Si. In general, the range of dSi concentrations seen in surface waters
622 of the ocean is lower than for lacustrine systems: ML lake waters, for example, reach
623 ~18 mg/L (> 600 μM; Table 2). Lake systems thus offer a chance to investigate a
624 potential dSi concentration dependency of diatom Si isotope fractionation. Figure 8

625 compiles diatom fractionations from this study and the published literature as a function
626 of water dSi concentration and temperatures. Two conclusions can be drawn. First, our
627 isotope fractionations estimated from coupled bSi-dSi $\delta^{30}Si$ for ML are the largest
628 magnitude reported to date. Note that they are also corroborated by the suite of water
629 samples alone (Figure 7; Table 2), which plot on a line defined by a fractionation of ca.
630 -3.5‰. Second, although these are also the datapoints at the highest dSi concentration,
631 there is no relationship between dSi concentration and the magnitude of diatom Si
632 isotope fractionation across the entirety of the data (Figure 8A). This corroborates
633 earlier conclusions in the marine realm (Sutton et al., 2013). Considering just the
634 freshwater estimates, a negative trend emerges but is strongly influenced by the two
635 ML datapoints. Future work could investigate diatom Si isotope fractionation in other
636 high dSi lacustrine environments. Most of the studies compiled in Figure 8 do not
637 generate diatom relative abundance counts. In the following, we explore the extent to
638 which we can exploit diatom assemblage data to yield insight into Si isotope
639 geochemistry.

640 Culturing experiments provide evidence that diatom silicon isotope
641 fractionation is not a constant value, even for the same taxa grown in similar (though
642 not identical) conditions (De La Rocha et al., 1997; Meyerink et al., 2017; Milligan et
643 al., 2004; Sutton et al., 2013). In the modern ocean, there are latitudinal gradients in
644 marine diatom Si isotope fractionation (Cardinal et al., 2007), which may reflect species
645 effects. There is also evidence that diatom fractionations at a single site change as the
646 community composition changes (e.g. Annett et al., 2017). Why different taxa have
647 different fractionations, or why the same species can exhibit different fractionations is
648 unclear, but some of the variability in natural settings may be related to trace-element

availability. For example, Fe availability has been shown to alter diatom Si isotope fractionation in some cases (Meyerink et al., 2017). There is also evidence that micronutrient (Fe, Zn, Cu, etc.) availability affects diatom cell stoichiometry (e.g. Baines et al., 2011) or frustule structure (e.g. Boutorh et al., 2016). Deconvolving intrinsic differences in Si metabolism between taxa, from changes induced by environmental variables, is important for accurate interpretation of paleoenvironmental records. Given that the high dSi concentrations in ML are indicative of hydrothermal fluids in the lake catchment, it is plausible that there is also an enhanced supply of trace-elements that may be enriched in hydrothermal fluids. We thus speculate that the large fractionations are linked to some facet of the water chemistry, and to hydrothermalism in the region (Ingebritsen et al., 2016).

Our modern and downcore assemblage data allows us to explore the role of diatom community composition in setting the net Si isotope fractionation factor. NMDS and indicator species analyses on all samples (from all three lakes) demonstrate that systematic and statistically significant relationships can be drawn between diatom assemblages and their $\delta^{30}Si_{bSi}$ (Figure 6, Table 3). Samples with the lowest $\delta^{30}Si_{bSi}$ values (< -1.1‰) are associated with Group 5, composed of araphid euplankton taxa *F. crotonensis, F. mesolepta*, such as seen in the Manzanita Lake plankton samples, and the Spring 2014 Butte Lake plankton sample. Samples with $\delta^{30}Si_{bSi}$ values -0.69 to -1.1‰ are associated mainly with Group 4, composed of araphid tychoplanktic taxa (i.e., *S. construens var venter, Pseudostaurosira brevistriata*), which are common throughout the Manzanita Lake core and the upper 45 cm of the Butte Lake core (Figure 5). Samples with moderate $\delta^{30}Si_{bSi}$ values (-0.55 to -0.66 ‰) are mainly associated with Group 3, a mixed group of attached periphyton, consisting of monoraphid taxa (i.e.,

673 *Karayevia clevei, Achnanthidium exiguum*) and araphid taxa (i.e., *Pseudostaurosira*
674 *parasitica, Staurosirella pinnata*), found in greatest abundance in a subset of Butte
675 Lake core samples (Figure 5). Samples with the highest $\delta^{30}Si_{bSi}$ values (> -0.14 ‰) are
676 mainly associated with Group 1, that comprise unattached, motile benthic, biraphid taxa
677 (i.e., *Navicula* spp, *Encyonopsis* spp, *Stauroneis* spp), and a few centric, euplanktic taxa
678 (i.e., *Discostella stelligera* and *Lindavia* spp), found in modern samples from Lower
679 Manzanita Creek and well as a subset of the Widow Lake core samples and Widow
680 Lake modern plankton sample (Figures 5,6). Although not significant at the $\alpha = 0.05$
681 level, araphid, needle-like Fragilaroid taxa are associated with low to moderate $\delta^{30}Si_{bSi}$
682 values (-0.21 to -0.51 ‰) (Table 3).

683 A-values for significant MRPP tests (Supplementary Material) reflect moderate
684 to large effects ranging from 0.095 to 0.455 for group separation, and within group
685 heterogeneity since dispersion within groups is variable (Figure 6). Thus, samples in a
686 given group (samples with similar range of $\delta^{30}Si_{bSi}$ values) are more like one another in
687 terms of specific diatom taxa than if they belonged to a different group (samples with
688 a different range of $\delta^{30}Si_{bSi}$ values). Pairwise comparisons of adjacent groups are not
689 significant at the $\alpha = 0.05$ level (1 v. 2, 2 v. 3, 3 v. 4) suggesting a degree of gradation
690 between these adjacent groups. Pairwise comparisons of non-adjacent groups (e.g.
691 Group 1 v. Group 3), which are separated by more than ~0.4‰ variation in $\delta^{30}Si$ value,
692 are significant at the $\alpha = 0.05$ level, indicating a clear distinction in their taxonomic
693 composition and demonstrating that species-specific isotope effects for different
694 functional groups can be teased out of whole-assemblage data in a quantitative manner.
695 Because these functional groups can be related to specific habitats (see above), the
696 contribution of potential micro-habitat effects on diatom Si isotope fractionation – for

example, via micronutrient availability, growth rate, ecological interactions, etc. - rather than intrinsic species-specific effects – cannot be strictly ruled out.

5.3 Si mass-balance for Manzanita Lake

Manzanita Lake is an efficient Si sink, removing approximately 30% of inflowing dSi. This conclusion is based on three independent lines of evidence: 1) the construction of elemental Si mass balance calculations (Figure 9, see below); 2) the isotope ratio difference between inflows and outflows and 3) sediment accumulation rates of bSi.

dSi concentration data and stream discharge data (Supplementary Material) allow the total mass of Si retained in the system to be derived (Figure 9). The reduction in fluvial dSi concentrations between upper and lower Manzanita Creeks is approximately 35%. Combined with an estimate of UMC discharge (Supplementary Material), this suggests a basin wide accumulation rate of ~0.008 g/m^2/yr. We measured δ^{30}Si = 1.01‰ in UMC and δ^{30}Si = 1.86‰ in LMC (Table 2). If we take an estimate $\varepsilon_{diat} \approx$ -2.5‰, based on isotope differences of the LAVO dSi-bSi sample pairs (section 5.2), this produces an estimate of 34% retention under the steady-state model and 29% for the Rayleigh model (Eqn. 1 and Eqn. 2, respectively). This agrees remarkably well with the estimate based on element fluxes alone (ca. 35%, see above and Figure 9). One implication is that any unaccounted for dSi inputs to the system (notably groundwater or soil-interflow water, plus potential direct hydrothermal fluid recirculation, though we have no evidence for this) has the same dSi concentration and δ^{30}Si as UMC waters. Were this not the case, the good agreement between the two methods would be unlikely.

Down-core percent bSi and average mass accumulation rates (based on core chronology data presented in Howard (2018)), produce an average bSi mass

721 accumulation rate (MAR) for recent ML lake sediments of ~0.023 g/m^2/yr (Figure 9).
722 This is approximately a factor of three higher than the estimate based on Si
723 concentrations. Two aspects may contribute to this discrepancy. Firstly, the fluvial dSi
724 flux does not represent 100% of the inputs of Si to ML. Other potential Si sources were
725 not quantified and therefore could contribute to the 'missing' dSi (see Figure 9).
726 Groundwater is likely the most important non-quantified flux, as it has been shown to
727 have high Si concentrations – often over 25 mg/L Si – in volcanic regions (Rosen,
728 2001; Schopka and Derry, 2012). Although the groundwater flux (implicitly including
729 Si derived from hydrothermal activity) is unknown for ML, it is expected to be an
730 important component of ML hydrology and as a source of Si for this system. The input
731 of amorphous Si phases in UMC sediments and via dust deposition could also
732 contribute Si to the system, though this is likely to be small (Frings et al., 2014). There
733 is no evidence for direct hydrothermal vent features in the lakes, though this cannot be
734 conclusively ruled out. Secondly, we do not attempt to correct for sediment focusing –
735 the tendency of sediment to move to deeper areas of a lake. In other words, the bSi
736 MAR is likely overestimated here since the core derives from the lakes depocenter.
737 Work elsewhere has shown that single cores can distort estimates of mass-accumulation
738 rates (Dillon and Evans, 2001; Hilton, 1985; Likens and Davis, 1975).

739 Recent work has highlighted how not accounting for groundwater can give
740 extremely misleading or nonsensical lake Si mass-balances (Zahajská et al., 2021). One
741 benefit of silicon-isotope based estimates of lake Si retention is that they can help
742 reconcile the divergent Si burial rates derived from elemental mass-balance (0.008
743 g/m^2/yr) with those from burial rates (0.023 g/m^2/yr). Assuming other sources of Si are
744 limited (e.g. within-lake sediment dissolution), it suggests that groundwater is

745 supplying about two-thirds of the lake dSi, corroborating the work of (Zahajská et al.,
746 2021) who argue it should be considered in lake budgets more widely. One of the few
747 lake Si mass-balances that explicitly consider groundwater Si reported a groundwater
748 contribution of 70 % for an Argentine pampean lake (Miretzky and Cirelli, 2004).
749 Elsewhere, (Hofmann et al., 2002) have acknowledged their Si mass-balance for Lake
750 Lugano, on the Swiss/Italian border, may be biased by the lack of groundwater data. In
751 a French crater lake, (Michard et al., 1994) have shown that groundwater supplies ca.
752 90% of dSi to the system. We thus suggest that analogously to the attention submarine
753 groundwater discharge is receiving for its importance to ocean element and isotopic
754 budgets (Mayfield et al., 2021; Rahman et al., 2019), the role of groundwater in
755 supplying nutrients to lake ecosystems should be more widely considered.

756 Harrison et al. (2012) and Frings et al. (2014) previously demonstrated that lake
757 hydraulic residence time is the most important control on lake Si retention efficiency.
758 There are several lake or reservoir systems with similar residence times to ML that have
759 established Si budgets. These include the reservoirs Alexandrina, Australia (ca. 3.6
760 months; Cook et al., 2010), Aube and Marne, France (ca. 4.8 and 5.5 months; Garnier
761 et al., 1999) and the natural systems Loch Leven, Scotland (ca. 5 months; Bailey-Watts
762 et al., 1989) and Southern Indian Lake, Canada (ca. 2.75 months; Hecky et al., 1986)).
763 These systems all have dSi retention efficiencies of a similar magnitude (mean ± 1σ =
764 44 ± 17%). Elsewhere, silicon isotopes have been used to quantify Si retention in Lake
765 Myvatn, Iceland (Opfergelt et al., 2011). Here, an elevated $\delta^{30}Si$ of lake outflow dSi,
766 by 0.2 – 0.9‰, relative to the dSi sources, was interpreted to reflect substantial Si
767 retention, even in a system with a water residence time of ~27 days (Opfergelt et al.,
768 2011). Zahajská et al. (2021) present a similar Si isotope mass-balance for the high

769 latitude, subarctic Lake 850 in northern Sweden, which retains ca. 79% of inflowing
770 dSi. These studies all point to the remarkable ability of lakes to quickly and efficiently
771 sequester dSi in their sediments as bSi. Seen in the context of this previous work, the
772 retention efficiency of Si in the sediments of ML, while large, is entirely in line with
773 other systems, both man-made and natural. Overall, this underscores the importance of
774 lacustrine systems in modifying both the riverine dSi flux and its silicon isotope
775 composition. It also demonstrates that silicon isotope geochemistry is a powerful tool
776 to quantify lake Si retention efficiency (Opfergelt et al., 2011; Zahajská et al., 2021).
777 Frings et al. (2014) estimated that lakes retain, as bSi in their sediments, about
778 25% of the Si flux released to the fluvial system from silicate weathering reactions.
779 Assuming the canonical diatom Si isotope fractionation of -1.1‰, this was sufficient to
780 raise riverine δ^{30}Si by 0.3‰ and arguably require consideration in paleoceanographic
781 studies. If the mean fractionation is actually closer to those observed in the LAVO
782 systems (-3.90 - -1.58‰; see above) then the impact on river δ^{30}Si would be
783 correspondingly greater and the δ^{30}Si of dSi delivered to the ocean on glacial-
784 interglacial timescales more sensitive to changing lake Si retention efficiency (Frings
785 et al., 2016)

786 **6. Conclusions**

787 Lakes act as biogeochemical reactors in the continental Si cycle, and efficiently
788 retain dSi in their sediments. Here, we used geochemical and (paleo)ecological
789 approaches to investigate Si cycling in three lakes in Lassen Volcanic National Park,
790 California. We generated data on lake characteristics, silicon isotope compositions, and
791 diatom abundances from modern and sediment core samples for Manzanita, Butte, and
792 Widow Lakes. These systems exhibit a range of diatom Si isotope fractionations,

793 including the largest reported to date. There are strong, significant relationships
794 between diatom species composition and diatom silicon isotope composition that were
795 revealed by ecological dimension-reducing statistical approaches. Samples that are
796 dominated by specific diatom functional groups tend to cluster within a specific range
797 of $\delta^{30}Si_{bS}$ values. These functional groups can be related to specific habitats. The
798 possibility of micro-habitat effects thus cannot be excluded as an explanation for
799 differences in $\delta^{30}Si_{bSi}$ values between species, rather than species-specific Si isotope
800 fractionation factors *sensu stricto*. Data from LAVO lake cores suggest that diatom
801 species composition most closely covaries with $\delta^{30}Si_{bSi}$ values over the past century.
802 While nutrient supply does play a role, the relationship between productivity and
803 $\delta^{30}Si_{bSi}$ is likely more indirect, mediated by the effects nutrient concentration and
804 stoichiometry have on the species composition of the sample. Finally, a Si mass-balance
805 for Manzanita Lake highlights the Si retention efficiency of lacustrine systems and
806 suggests an understudied role for groundwater in lake dSi supply.

807 **7. Acknowledgments**

808 This project was funded by the George Melendez Wright Climate Change Fellowship,
809 the Geological Society of America to Kerry Schmidtbauer (formerly Kerry Howard).
810 This work was partially supported by a grant from the Knut and Alice Wallenberg
811 Foundation, by the Swedish Research Council (VR), and the European
812 Community's Horizon 2020 Program/ERC Advanced Grant #833454 to Daniel J.
813 Conley. Thanks to the National Park Service and LAVO staff, to Eric Dinger (Klamath
814 Network Inventory and Monitoring Program, National Park Service), Scott Mensing
815 for assistance in Coring Butte and Manzanita lakes, LacCore for access to facilities for
816 core processing and analysis, and to Briana Johnson, Paige DePolo, Dave Kreamer,
817 Wes Rubio, Bud Schmidtbauer, and Sarah Luse for assisting in fieldwork. We thank
818 Nicole Fernandez and an anonymous reviewer for their constructive and valuable
819 comments on an earlier version of this manuscript, and Jérôme Gaillardet for editorial
820 handling.

821 **8. Figure captions**

***Figure 1*:** Locations of Manzanita, Butte, and Widow Lakes and catchment areas in Lassen Volcanic National Park, California.

***Figure 2*:** Three isotope plot of $\delta^{30}Si$ and $\delta^{29}Si$ values of water, modern diatom samples, and bulk sediment core biogenic silica (diatom) for LAVO lakes. The gradient of the linear regression between $\delta^{30}Si$ and $\delta^{29}Si$ agrees with theoretical predictions of the mass-dependency of Si isotopes, indicating the successful removal of polyatomic interferences during sample preparation and measurement (see main text for details). A long-term reproducibility of ±0.15 ‰ (2sd) is shown; typical internal measurement precisions are better.

***Figure 3*:** Vertical profiles of temperature (°C), dissolved oxygen (mg/L), and specific conductance (µS/cm), taken on 7 sampling dates in 2012-2014 for: Column A) Manzanita Lake, and Column B) Widow Lake. Colors indicate the months that samples were collected in each year.

Figure 4: Down-core plots of sediment core $\delta^{30}Si_{bSi}$, sedimentary bSi concentrations, and diatom taxa relative abundances for Manzanita, Widow, and Butte lakes. Vertical axes are: calendar year per ^{210}Pb age model, and cm below lake floor. Age models for each core can be found in the online Supplementary Material. Epi = Epilithic, Ben = Benthic, Peri = Periphyton. Diatom taxa abbreviations, corresponding to those in Howard (2018), are ACHN = *Achnanthidium* spp., AMIN = *Achnanthidium minutissimum*, ADLA = *Adlafia* spp., AGVA = *Aulacoseira granulata* var. *angustissima*, AULA = *Aulacoseira* spp. 4, AFOR = *Asterionella formosa*, DIAT = *Diatoma mesodon*, DINC = *Distrionella incognita,* DSTE = *Discostella stelligera*, ENPS1 = *Encyonopsis* spp. 4, FCRO = *Fragilaria crotonensis*, FGRU = *Fragilaria grunowii*, FMES = *Fragilaria mesolepta,* FPED = *Fragilaria perdelicatissima*, FTEU = *Fragilaria tenuissima*, FVAU = *Fragilaria vaucheriae,* GOMP1 = *Gomphonema* spp. 1, KCLE = *Karayevia clevei*, LIND = *Lindavia* spp., NAVI1 = *Navicula* spp. 1, NITZ = *Nitzschia spp.,* NLIE = *Nitzschia liebertruthii*, NPER = *Nitzschia perminuta*, PINN3 = *Pinnularia* spp. 3, PINN4 = *Pinnularia* spp. 4, PBRE = *Pseudostaurosira brevistriata*, PPAR = *Pseudostaurosira parasitica* , PSEU = *Pseudostaurosira pseudoconstruens*, REIS = *Reimeria sinuata,* SPUP = *Sellaphora pupula*, SCVB = *Staurosira construens* var. *binodis*, SCVV = *Staurosira construens* var. *venter*, SPIN = *Staurosirella pinnata*, SNEO = *Stauroneis neohyalina*, SANC = *Stauroneis anceps*, STEP = *Stephanodiscus* spp., STEPH1 = *Stephanodiscus* sp. 1, STEPH2 = *Stephanodiscus* sp. 2, TFLO = *Tabellaria flocculosa.*

Figure 5: Vertical profiles of lake $\delta^{30}Si_{dSi}$ values for Manzanita and Butte lakes in 2014. Manzanita Creek inflow values are used for surface water in UMC as a background reference because groundwater values of $\delta^{30}Si_{dSi}$ are unknown. Consistently higher lake $\delta^{30}Si$ than inflow values for ML indicates biological utilization of dSi. Generally higher surface water $\delta^{30}Si$ than deeper waters indicates biosiliceous production at the surface and progressive dissolution in the water column or sediments, though vertical mixing occasionally obscures this general pattern. A long-term reproducibility of ±0.15 ‰ (2sd) is shown; typical internal measurement precisions are better.

***Figure 6*:** NMDS biplot of Axis 1 v. Axis 3 for modern and down-core samples overlain

with convex hulls of five groups of $\delta^{30}Si_{bSi}$ values (determined by constrained clustering). The samples assigned to each group are plotted by symbol. The range of $\delta^{30}Si_{bSi}$ values for each of the groups is found in table 3, as are the indicator taxa associated with each group. Axis 1 explains 43% of the variance, Axis 3 explains 18% of the variance. The statistical analyses indicate that approaches designed for the analysis of noisy, ecological data can be used to deconvolve species-specific isotope effects from bulk samples.

***Figure 7*:** Evolution of silicon isotope ratios in Manzanita Lake in samples from 2014 as a function of fraction of dSi converted to bSi by diatom growth. The x-axis (C/C_0) is taken as a proxy for relative fraction of reactant (dSi) remaining, where C is the dSi concentration ML waters, and C_0 the initial concentration in inflow UMC waters (see values in Table 2 and main text for details). Vertical arrows indicate the isotope difference between bSi and dSi samples collected simultaneously. Black and red lines indicate the predicted evolution of $\delta^{30}Si$ as a function of f_{Si} for the Rayleigh (Eqn. 1) and Steady-State (Eqn. 2) models, respectively. A long-term reproducibility of ±0.15 ‰ (2sd) is shown; typical internal measurement precisions are better.

***Figure 8*:** A compilation of diatom Si isotope fractionations from the literature for freshwater (green symbols), estuarine/brackish (light blue symbols), and marine (dark blue symbols) environments, as a function of A) dSi concentration and B) temperature. Symbol shape indicates study type: laboratory/culturing experiment (squares); mesocosm experiment (diamonds), and empirical field measurements (circles). Many of the field-based studies are displayed as two symbols if the original study did not or could not differentiate between Rayleigh and Steady-State models. The lack of a correlation between magnitude of isotope fractionation and either dSi concentration or temperature indicates the variation in fractionation remains to be explained and may be partially related to species specific Si processing pathways. DLR97 refers to the De La Rocha et al. (1997) canonical value for diatom Si isotope fractionation of -1.1‰. Data from this study and literature (Alleman et al., 2005; Annett et al., 2017; Beucher et al., 2008; Beucher et al., 2011; Cao et al., 2015; Cao et al., 2012; Cassarino et al., 2017; Closset et al., 2015; Closset et al., 2019; Coffineau et al., 2014; De La Rocha et al., 1997; Doering et al., 2016; Egan et al., 2012; Ehlert et al., 2012; Fripiat et al., 2007; Meyerink et al., 2017; Meyerink et al., 2019; Milligan et al., 2004; Opfergelt et al., 2011; Panizzo et al., 2017; Reynolds et al., 2006; Sun et al., 2013; Sun et al., 2018; Sun et al., 2014; Sutton et al., 2013; Varela et al., 2016; Varela et al., 2004; Weiss et al., 2015; Zhang et al., 2015; Zhang et al., 2020).

***Figure 9*:** Simple mass-balance model for Si in Manzanita Lake, as described in main text. Retention efficiency based on Si concentrations observed in surface inflow and outflow in 2014, and agrees well with isotope-based estimate (see main text and Figure 7). These can be scaled to burial fluxes by using field measurements (2014) of surface inflow/outflow rate (slope-area method; Supplementary Material) and/or historical USGS gauging data (1979-81 Lower Manzanita Creek; Supplementary Material). For comparison, an estimate of average bSi (from down-core bSi concentrations) mass accumulation rate (based on ^{210}Pb and ^{137}Cs-derived sediment accumulation rate for ML lake gravity core, data from Howard (2018)) is presented. Sediment-core derived burial fluxes are a factor of three higher than lake mass-balance derived fluxes, which

910 may be due to groundwater dSi supply, to sediment focusing, or to a combination.

911 **10. Table captions**

912 ***Table 1***: Table 1: Summary of Manzanita, Butte, and Widow lakes catchment
913 characteristics and morphometry. For closed or semi-closed lakes (BL, WL), size
914 metrics calculated based on GIS data representing full-lake conditions (see Howard and
915 Noble 2018). Curve Number is an empirical parameter that predicts the likelihood of
916 overland runoff for a rainfall event; Shoreline Development is shoreline length relative
917 to a circle of the same area. Notes: [1]Small ephemeral stream; a dry stream bed indicated
918 a potential inflow, but no flow was observed during the 2012-2014 sampling period.
919 [2]Lower Manzanita Creek sampled by USGS 1979-1981, data accessed via NWIS
920 portal, site number: 11376038. [3]Outflow in Butte Creek was observed May-September
921 in 2012. In 2013/2014, Butte Lake level dropped below the outflow level and outflow
922 ceased. [4]Although a dry creek/stream bed indicated a possible inflow path; no flow was
923 observed during sampling activities 2012-2014. [5]See discussion in Howard and Noble
924 (2018)

925 ***Table 2***: Table 2: Modern silicon concentrations (mg/l) and $\delta^{30}Si$ values for lake water
926 dSi and diatom bSi , and observed Chl-a and Secchi depth values for BL, ML, and WL
927 on sampling dates in 2012-2014. Range, Mean, and SD for ML do not include UMC
928 and LMC values. Long term typical reproducibility on $\delta^{30}Si$ data is ±0.15 (2σ). Notes:
929 *Secchi depth was estimated by measuring visible depth to white 2L Van Dorn water
930 sampler. [1]$\delta^{30}Si_{bSi}$ values presented for 2014-05-29 and 2014-09-26 are for periphyton
931 taxa collected from surface scrapes.

932 ***Table 3*****:** Significant ($\alpha < 0.05$) indicator taxa for Groups 1, 3, 4, 5 (Groups based on
933 groupings determined from $\delta^{30}Si$ values). Although not significant, top taxa for Group
934 2 are also given. IV = indicator value. Taxa listed in this table also are shown in figure
935 4, along with their habitat associations.

936 **11. References**

937 Abelmann, A., Gersonde, R., Knorr, G., Zhang, X., Chapligin, B., Maier, E., Esper, O.,
938 Friedrichsen, H., Lohmann, G. and Meyer, H. (2015) The seasonal sea-ice zone in the
939 glacial Southern Ocean as a carbon sink. Nature Communications 6.

940 Alleman, L.Y., Cardinal, D., Cocquyt, C., Plisnier, P.D., Descy, J.P., Kimirei, I.,
941 Sinyinza, D. and Andre, L. (2005) Silicon isotopic fractionation in Lake Tanganyika
942 and its main tributaries. J. Gt. Lakes Res. 31, 509-519.

943 Annett, A.L., Henley, S.F., Venables, H.J., Meredith, M.P., Clarke, A. and Ganeshram,
944 R.S. (2017) Silica cycling and isotopic composition in northern Marguerite Bay on the
945 rapidly-warming western Antarctic Peninsula. Deep Sea Research Part II: Topical
946 Studies in Oceanography 139, 132-142.

947 Appleby, P.G. (2001) Chronostratigraphic techniques in recent sediments, in: Last,
948 W.M., Smol, J.P. (Eds.), Tracking Environmental Change Using Lake Sediements,
949 Volume 1: Basin Analysis, Coring and Chronological Techniques. Kluwer, London,
950 pp. 171-204.

951 Appleby, P.G. and Oldfield, F. (1978) The calculation of lead-210 dates assuming a
952 constant rate of supply of unsupported 210Pb to the sediment. Catena 5, 1-8.

953 Bailey-Watts, A.E., Smith, I.R. and Kirika, A. (1989) The dynamics of silica in a
954 shallow, diatom-rich Scottish Loch I: stream inputs of the dissolved nutrient. Diatom
955 Research 4, 179-190.

956 Baines, S.B., Twining, B.S., Vogt, S., Balch, W.M., Fisher, N.S. and Nelson, D.M.
957 (2011) Elemental composition of equatorial Pacific diatoms exposed to additions of
958 silicic acid and iron. Deep Sea Research Part II: Topical Studies in Oceanography 58,
959 512-523.

960 Battarbee, R.W., Jones, V.J., Flower, R.J., Cameron, N.G., Bennion, H., Carvalho, L.
961 and Juggins, S. (2001) Diatoms., in: Smol, J.P., Birks, H.J.B., Last, W.M. (Eds.),
962 Tracking Environmental Change Using Lake Sediments, Volume 3: Terrestrial, Algal
963 and Siliceous Indicators. Kluwer, London, pp. 155-202.

964 Beucher, C.P., Brzezinski, M.A. and Jones, J.L. (2008) Sources and biological
965 fractionation of Silicon isotopes in the Eastern Equatorial Pacific. Geochimica et
966 Cosmochimica Acta 72, 3063-3073.

967 Beucher, C.P., Brzezinski, M.A. and Jones, J.L. (2011) Mechanisms controlling silicon
968 isotope distribution in the Eastern Equatorial Pacific. Geochimica et Cosmochimica
969 Acta 75, 4286-4294.

970 Borcard, D., Gillet, F. and Legendre, P. (2018) Numerical ecology with R. Springer.

971 Boutorh, J., Moriceau, B., Gallinari, M., Ragueneau, O. and Bucciarelli, E. (2016)
972 Effect of trace metal- limited growth on the postmortem dissolution of the marine
973 diatom Pseudo- nitzschia delicatissima. Global Biogeochemical Cycles 30, 57-69.

974 Cao, Z., Frank, M. and Dai, M. (2015) Dissolved silicon isotopic compositions in the
975 E ast C hina S ea: Water mass mixing vs. biological fractionation. Limnology and
976 Oceanography 60, 1619-1633.

977 Cao, Z., Frank, M., Dai, M., Grasse, P. and Ehlert, C. (2012) Silicon isotope constraints
978 on sources and utilization of silicic acid in the northern South China Sea. Geochimica
979 et Cosmochimica Acta 97, 88-104.

980 Cardinal, D., Alleman, L.Y., de Jong, J., Ziegler, K. and Andre, L. (2003) Isotopic
981 composition of silicon measured by multicollector plasma source mass spectrometry in
982 dry plasma mode. Journal of Analytical Atomic Spectrometry 18, 213-218.

983 Cardinal, D., Savoye, N., Trull, T.W., Dehairs, F., Kopczynska, E.E., Fripiat, F., Tison,
984 J.L. and Andre, L. (2007) Silicon isotopes in spring Southern Ocean diatoms: Large
985 zonal changes despite homogeneity among size fractions. Mar. Chem. 106, 46-62.

986 Cassarino, L., Coath, C.D., Xavier, J.R. and Hendry, K.R. (2018) Silicon isotopes of
987 deep sea sponges: new insights into biomineralisation and skeletal structure.
988 Biogeosciences 15, 6959-6977.

989 Cassarino, L., Hendry, K.R., Meredith, M.P., Venables, H.J. and De La Rocha, C.L.
990 (2017) Silicon isotope and silicic acid uptake in surface waters of Marguerite Bay, West
991 Antarctic Peninsula. Deep Sea Research Part II: Topical Studies in Oceanography 139,
992 143-150.

993 Chen, J., Li, J., Tian, S., Kalugin, I., Darin, A. and Xu, S. (2012) Silicon isotope
994 composition of diatoms as a paleoenvironmental proxy in Lake Huguangyan, South
995 China. Journal of Asian Earth Sciences 45, 268-274.

996 Closset, I., Cardinal, D., Bray, S.G., Thil, F., Djouraev, I., Rigual- Hernández, A.S.
997 and Trull, T.W. (2015) Seasonal variations, origin, and fate of settling diatoms in the
998 Southern Ocean tracked by silicon isotope records in deep sediment traps. Global
999 Biogeochemical Cycles 29, 1495-1510.

1000 Closset, I., Cardinal, D., Rembauville, M., Thil, F. and Blain, S. (2016) Unveiling the
1001 Si cycle using isotopes in an iron-fertilized zone of the Southern Ocean: from mixed-
1002 layer supply to export. Biogeosciences 13, 6049-6066.

1003 Closset, I., Cardinal, D., Trull, T.W. and Fripiat, F. (2019) New insights into processes
1004 controlling the δ30Si of sinking diatoms: A seasonally resolved box model approach.
1005 Global Biogeochemical Cycles 33, 957-970.

1006 Clynne, M., Champion, D., Trimble, D., Hendley II, J. and Stauffer, P. (2000) How Old
1007 is “Cinder Cone”? Solving a Mystery in Lassen Volcanic National Park, California US
1008 Geological Survey Fact Sheet, 023-000.

1009 Clynne, M.A., Christiansen, R.L., Trimble, D.A. and McGeehin, J.P. (2008)
1010 Radiocarbon dates from volcanic deposits of the Chaos Crags and Cinder Cone eruptive
1011 sequences and other deposits, Lassen Volcanic National Park and vicinity, California.
1012 US Geological Society Open-File Report, 02-290.

1013 Clynne, M.A. and Muffler, L.J.P. (2010) Geologic map of Lassen Volcanic National

1014 Park and vicinity, California. US Department of the Interior, US Geological Survey.

1015 Clynne, M.A., Robinson, J.E., Nathenson, M. and Muffler, L.P. (2012) Volcano
1016 hazards assessment for the Lassen region, northern California. US Department of the
1017 Interior, US Geological Survey.

1018 Cockerton, H.E., Street-Perrott, F.A., Barker, P.A., Leng, M.J., Sloane, H.J. and Ficken,
1019 K.J. (2015) Orbital forcing of glacial/interglacial variations in chemical weathering and
1020 silicon cycling within the upper White Nile basin, East Africa: Stable-isotope and
1021 biomarker evidence from Lakes Victoria and Edward. Quaternary Science Reviews
1022 130, 57-71.

1023 Coffineau, N., De La Rocha, C.L. and Pondaven, P. (2014) Exploring interacting
1024 influences on the silicon isotopic composition of the surface ocean: a case study from
1025 the Kerguelen Plateau. Biogeosciences 11, 1371-1391.

1026 Cook, P., Aldridge, K., Lamontagne, S. and Brookes, J. (2010) Retention of nitrogen,
1027 phosphorus and silicon in a large semi-arid riverine lake system. Biogeochemistry 99,
1028 49-63.

1029 Coplen, T.B. (2011) Guidelines and recommended terms for expression of stable-
1030 isotope- ratio and gas- ratio measurement results. Rapid Commun. Mass Spectrom.
1031 25, 2538-2560.

1032 Dalrymple, T. and Benson, M. (1968) Measurement of peak discharge by the slope-
1033 area method. US Government Printing Office.

1034 De La Rocha, C.L., Brzezinski, M.A. and DeNiro, M.J. (1996) Purification, Recovery,
1035 and Laser-Driven Fluorination of Silicon from Dissolved and Particulate Silica for the
1036 Measurement of Natural Stable Isotope Abundances. Analytical Chemistry 68, 3746-
1037 3750.

1038 De La Rocha, C.L., Brzezinski, M.A. and DeNiro, M.J. (1997) Fractionation of silicon
1039 isotopes by marine diatoms during biogenic silica formation. Geochimica et
1040 Cosmochimica Acta 61, 5051-5056.

1041 De La Rocha, C.L., Brzezinski, M.A., DeNiro, M.J. and Shemesh, A. (1998) Silicon-
1042 isotope composition of diatoms as an indicator of past oceanic change. Nature 395, 680-
1043 683.

1044 Dillon, P.J. and Evans, H.E. (2001) Comparison of iron accumulation in lakes using
1045 sediment core and mass balance calculations. Science of The Total Environment 266,
1046 211-219.

1047 Doering, K., Ehlert, C., Grasse, P., Crosta, X., Fleury, S., Frank, M. and Schneider, R.
1048 (2016) Differences between mono-generic and mixed diatom silicon isotope
1049 compositions trace present and past nutrient utilisation off Peru. Geochimica et
1050 Cosmochimica Acta 177, 30-47.

1051 Dufrêne, M. and Legendre, P. (1997) Species assemblages and indicator species: the
1052 need for a flexible asymmetrical approach. Ecological Monographs 67, 345-366.

1053 Eakins, J.a. and Morrison, R. (1978) A new procedure for the determination of lead-
1054 210 in lake and marine sediments. The International Journal of Applied Radiation and
1055 Isotopes 29, 531-536.

1056 Egan, K.E., Rickaby, R.E.M., Leng, M.J., Hendry, K.R., Hermoso, M., Sloane, H.J.,
1057 Bostock, H. and Halliday, A.N. (2012) Diatom silicon isotopes as a proxy for silicic
1058 acid utilisation: A Southern Ocean core top calibration. Geochimica et Cosmochimica
1059 Acta 96, 174-192.

1060 Ehlert, C., Grasse, P., Mollier-Vogel, E., Böschen, T., Franz, J., de Souza, G.F.,
1061 Reynolds, B.C., Stramma, L. and Frank, M. (2012) Factors controlling the silicon
1062 isotope distribution in waters and surface sediments of the Peruvian coastal upwelling.
1063 Geochimica et Cosmochimica Acta 99, 128-145.

1064 Engström, E., Rodushkin, I., Baxter, D.C. and Öhlander, B. (2005) Chromatographic
1065 Purification for the Determination of Dissolved Silicon Isotopic Compositions in
1066 Natural Waters by High-Resolution Multicollector Inductively Coupled Plasma Mass
1067 Spectrometry. Analytical Chemistry 78, 250-257.

1068 Frings, P.J. (2019) Palaeoweathering: How Do Weathering Rates Vary with Climate?
1069 Elements 15, 259-265.

1070 Frings, P.J., Clymans, W., Jeppesen, E., Lauridsen, T.L., Struyf, E. and Conley, D.J.
1071 (2014) Lack of steady-state in the global biogeochemical Si cycle: emerging evidence
1072 from lake Si sequestration. Biogeochemistry 117, 255-277.

1073 Frings, P.J., Fontorbe, G., Clymans, W., De La Rocha, C.L. and Conley, D.J. (2016)
1074 The continental Si cycle and its impact on the ocean Si isotope budget. Chemical
1075 Geology 425, 12-36.

1076 Fripiat, F., Cardinal, D., Tison, J.L., Worby, A. and André, L. (2007) Diatom- induced
1077 silicon isotopic fractionation in Antarctic sea ice. Journal of Geophysical Research:
1078 Biogeosciences 112.

1079 Garnier, J., Leporcq, B., Sanchez, N. and Philippon, X. (1999) Biogeochemical mass-
1080 balances (C, N, P, Si) in three large reservoirs of the Seine Basin (France).

1081 Biogeochemistry 47, 119-146.

1082 Glew, J., Smol, J. and Last, W. (2001) Tracking environmental change using lake
1083 sediments: Basin analysis, coring, and chronological techniques.

1084 Harrison, J.A., Frings, P.J., Beusen, A.H.W., Conley, D.J. and McCrackin, M.L. (2012)
1085 Global importance, patterns, and controls of dissolved silica retention in lakes and
1086 reservoirs. Global Biogeochemical Cycles 26, GB2037.

1087 Hecky, R.E., Kling, H.J. and Brunskill, G.J. (1986) Seasonality of phytoplankton in
1088 relation to silicon cycling and interstitial water circulation in large, shallow lakes of
1089 Central Canada. Hydrobiologia 138, 117-126.

1090 Hendry, K.R. and Robinson, L.F. (2012) The relationship between silicon isotope
1091 fractionation in sponges and silicic acid concentration: Modern and core-top studies of
1092 biogenic opal. Geochimica et Cosmochimica Acta 81, 1-12.

1093 Hilton, J. (1985) A conceptual-framework for predicting the occurrence of sediment
1094 focusing and sediment redistribution in small lakes. Limnology and Oceanography 30,
1095 1131-1143.

1096 Hofmann, A., Roussy, D. and Filella, M. (2002) Dissolved silica budget in the North
1097 basin of Lake Lugano. Chemical Geology 182, 35-55.

1098 Howard, K. and Noble, P. (2018) Hydrological perturbations drive rapid shifts in
1099 phytoplankton biodiversity and population dynamics in Butte Lake (Lassen Volcanic
1100 National Park, California). Lake Reserv. Manag. 34, 21-41.

1101 Howard, K.L. (2018) Neo and paleo-limnological response to nutrient, climate, and
1102 volcanic stressors over the past 100 years at Butte, Manzanita, and Widow lakes in
1103 Lassen Volcanic National Park (CA, USA).

1104 Ingebritsen, S.E., Bergfeld, D., Clor, L.E. and Evans, W.C. (2016) The Lassen
1105 hydrothermal system. American Mineralogist 101, 343-354.

1106 Juggins, S. and Juggins, M.S. (2020) Package 'rioja'.

1107 Kilham, P. (1971) A hypothesis concerning silica and the freshwater planktonic
1108 diatoms. Limnology and Oceanography 16, 10-18.

1109 Likens, G.E. and Davis, M.B. (1975) Post-Glacial History of Mirror Lake and Its
1110 Watershed In New Hampshire, U. S. A.: An Initial Report. Verhandlungen
1111 Internationale Vereinigung Limnologie 19, 982-993.

1112 Mayfield, K.K., Eisenhauer, A., Santiago Ramos, D.P., Higgins, J.A., Horner, T.J.,
1113 Auro, M., Magna, T., Moosdorf, N., Charette, M.A., Gonneea, M.E., Brady, C.E.,
1114 Komar, N., Peucker-Ehrenbrink, B. and Paytan, A. (2021) Groundwater discharge
1115 impacts marine isotope budgets of Li, Mg, Ca, Sr, and Ba. Nature Communications 12,
1116 148.

1117 McCune, B.P. and Grace, J. (2002) Analysis of Ecological Communities.

1118 Meyerink, S., Ellwood, M.J., Maher, W.A. and Strzepek, R. (2017) Iron availability
1119 influences silicon isotope fractionation in two Southern Ocean diatoms (Proboscia
1120 inermis and Eucampia Antarctica) and a coastal diatom (Thalassiosira pseudonana).
1121 Frontiers in Marine Science 4, 217.

1122 Meyerink, S.W., Boyd, P.W., Maher, W.A., Milne, A., Strzepek, R. and Ellwood, M.J.
1123 (2019) Putting the silicon cycle in a bag: Field and mesocosm observations of silicon
1124 isotope fractionation in subtropical waters east of New Zealand. Mar. Chem. 213, 1-12.

1125 Michard, G., Viollier, E., Jezequel, D. and Sarazin, G. (1994) Geochemical study of a
1126 crater lake - Pavin Lake, France - identification, location and quantification of the
1127 chemical-reactions in the lake. Chemical Geology 115, 103-115.

1128 Milligan, A.J., Varela, D.E., Brzezinski, M.A. and Morel, F. (2004) Dynamics of
1129 silicon metabolism and silicon isotopic discrimination in a marine diatom as a function
1130 of pCO(2). Limnology and Oceanography 49, 322-329.

1131 Miretzky, P. and Cirelli, A.F. (2004) Silica dynamics in a pampean lake (Lake
1132 Chascomus, Argentina). Chemical Geology 203, 109-122.

1133 Morley, D., Leng, M., Mackay, A., Sloane, H., Rioual, P. and Battarbee, R. (2004)
1134 Cleaning of lake sediment samples for diatom oxygen isotope analysis. Journal of
1135 Paleolimnology 31, 391-401.

1136 Mortlock, R.A. and Froelich, P.N. (1989) A simple method for the rapid determination
1137 of biogenic opal in pelagic marine sediments. Deep-Sea Research Part a-Oceanographic
1138 Research Papers 36, 1415-1426.

1139 Nantke, C.K.M., Brauer, A., Frings, P.J., Czymzik, M., Hübener, T., Stadmark, J.,
1140 Dellwig, O., Roeser, P. and Conley, D.J. (2021) Human influence on the continental Si
1141 budget during the last 4300 years: δ30Sidiatom in varved lake sediments (Tiefer See,
1142 NE Germany). Quaternary Science Reviews 258, 106869.

1143 Nantke, C.K.M., Frings, P.J., Stadmark, J., Czymzik, M. and Conley, D.J. (2019) Si
1144 cycling in transition zones: a study of Si isotopes and biogenic silica accumulation in
1145 the Chesapeake Bay through the Holocene. Biogeochemistry 146, 145-170.

1146 Oelze, M., Schuessler, J.A. and von Blanckenburg, F. (2016) Mass bias stabilization by
1147 Mg doping for Si stable isotope analysis by MC-ICP-MS. Journal of Analytical Atomic
1148 Spectrometry 31, 2094-2100.

1149 Opfergelt, S. and Delmelle, P. (2012) Silicon isotopes and continental weathering
1150 processes: Assessing controls on Si transfer to the ocean. Comptes Rendus Geoscience
1151 344, 723-738.

1152 Opfergelt, S., Eiriksdottir, E., Burton, K., Einarsson, A., Siebert, C., Gislason, S. and
1153 Halliday, A. (2011) Quantifying the impact of freshwater diatom productivity on silicon
1154 isotopes and silicon fluxes: Lake Myvatn, Iceland. Earth and Planetary Science Letters
1155 305, 73-82.

1156 Panizzo, V.N., Swann, G.E.A., Mackay, A.W., Vologina, E., Alleman, L., André, L.,
1157 Pashley, V.H. and Horstwood, M.S.A. (2017) Constraining modern-day silicon cycling
1158 in Lake Baikal. Global Biogeochemical Cycles 31, 556-574.

1159 Panizzo, V.N., Swann, G.E.A., Mackay, A.W., Vologina, E., Sturm, M., Pashley, V.
1160 and Horstwood, M.S.A. (2016) Insights into the transfer of silicon isotopes into the
1161 sediment record. Biogeosciences 13, 147-157.

1162 Parsons, T.R., Maita, Y. and Lalli, C.M. (1984) 4.2 - Spectrophotometric Determination
1163 of Phaeo-pigments, in: Parsons, T.R., Maita, Y., Lalli, C.M. (Eds.), A Manual of
1164 Chemical & Biological Methods for Seawater Analysis. Pergamon, Amsterdam, pp.
1165 104-107.

1166 Peck, J.E. (2016) Multivariate analysis for ecologists: step-by-step. MjM Software
1167 Design.

1168 Pourchet, M., Pinglot, J.F. and Mélières, M.A. (1989) Cesium 137 and Lead 210 in
1169 alpine lake sediments: measurements and modeling of mixing processes. Journal of
1170 Geophysical Research: Oceans 94, 12761-12770.

1171 Rahman, S., Tamborski, J.J., Charette, M.A. and Cochran, J.K. (2019) Dissolved silica
1172 in the subterranean estuary and the impact of submarine groundwater discharge on the
1173 global marine silica budget. Mar. Chem. 208, 29-42.

1174 Reynolds, B.C., Aggarwal, J., Andre, L., Baxter, D., Beucher, C., Brzezinski, M.A.,
1175 Engstrom, E., Georg, R.B., Land, M., Leng, M.J., Opfergelt, S., Rodushkin, I., Sloane,
1176 H.J., van den Boorn, S., Vroon, P.Z. and Cardinal, D. (2007) An inter-laboratory
1177 comparison of Si isotope reference materials. Journal of Analytical Atomic
1178 Spectrometry 22, 561-568.

1179 Reynolds, B.C., Frank, M. and Halliday, A.N. (2006) Silicon isotope fractionation

during nutrient utilization in the North Pacific. Earth and Planetary Science Letters 244, 431-443.

Rosen, M. (2001) Hydrochemistry of New Zealand's aquifers. New Zealand Hydrological Society.

Schopka, H.H. and Derry, L.A. (2012) Chemical weathering fluxes from volcanic islands and the importance of groundwater: the Hawaiian example. Earth and Planetary Science Letters 339, 67-78.

Stoermer, E.F., Edlund, M.B., Pilskaln, C.H. and Schelske, C.L. (1995) Siliceous microfossil distribution in the surficial sediments of Lake Baikal. Journal of Paleolimnology 14, 69-82.

Street-Perrott, F.A., Barker, P.A., Leng, M.J., Sloane, H.J., Wooller, M.J., Ficken, K.J. and Swain, D.L. (2008) Towards an understanding of late Quaternary variations in the continental biogeochemical cycle of silicon: multi-isotope and sediment-flux data for Lake Rutundu, Mt Kenya, East Africa, since 38 ka BP. Journal of Quaternary Science 23, 375-387.

Sun, X., Andersson, P.S., Humborg, C., Pastuszak, M. and Mörth, C.-M. (2013) Silicon isotope enrichment in diatoms during nutrient-limited blooms in a eutrophied river system. Journal of Geochemical Exploration 132, 173-180.

Sun, X., Mörth, C.-M., Porcelli, D., Kutscher, L., Hirst, C., Murphy, M.J., Maximov, T., Petrov, R.E., Humborg, C. and Schmitt, M. (2018) Stable silicon isotopic compositions of the Lena River and its tributaries: Implications for silicon delivery to the Arctic Ocean. Geochimica et Cosmochimica Acta 241, 120-133.

Sun, X., Olofsson, M., Andersson, P.S., Fry, B., Legrand, C., Humborg, C. and Mörth, C.-M. (2014) Effects of growth and dissolution on the fractionation of silicon isotopes by estuarine diatoms. Geochimica et Cosmochimica Acta 130, 156-166.

Sutton, J.N., Varela, D.E., Brzezinski, M.A. and Beucher, C.P. (2013) Species-dependent silicon isotope fractionation by marine diatoms. Geochimica et Cosmochimica Acta 104, 300-309.

Swann, G.E.A., Leng, M.J., Juschus, O., Melles, M., Brigham-Grette, J. and Sloane, H.J. (2010) A combined oxygen and silicon diatom isotope record of Late Quaternary change in Lake El'gygytgyn, North East Siberia. Quaternary Science Reviews 29, 774-786.

Varela, D., Brzezinski, M., Beucher, C., Jones, J., Giesbrecht, K., Lansard, B. and Mucci, A. (2016) Heavy silicon isotopic composition of silicic acid and biogenic silica

in Arctic waters over the Beaufort shelf and the Canada Basin. Global Biogeochemical Cycles 30, 804-824.

Varela, D.E., Pride, C.J. and Brzezinski, M.A. (2004) Biological fractionation of silicon isotopes in Southern Ocean surface waters. Global Biogeochemical Cycles 18.

Weiss, A., De La Rocha, C., Amann, T. and Hartmann, J. (2015) Silicon isotope composition of dissolved silica in surface waters of the Elbe Estuary and its tidal marshes. Biogeochemistry, 1-19.

Welschmeyer, N.A. (1994) Fluorometric analysis of chlorophyll a in the presence of chlorophyll b and pheopigments. Limnology and Oceanography 39, 1985-1992.

Wille, M., Sutton, J., Ellwood, M.J., Sambridge, M., Maher, W., Eggins, S. and Kelly, M. (2010) Silicon isotopic fractionation in marine sponges: A new model for understanding silicon isotopic variations in sponges. Earth and Planetary Science Letters 292, 281-289.

Zahajská, P., Olid, C., Stadmark, J., Fritz, S.C., Opfergelt, S. and Conley, D.J. (2021) Modern silicon dynamics of a small high-latitude subarctic lake. Biogeosciences 18, 2325-2345.

Zhang, A., Zhang, J., Hu, J., Zhang, R. and Zhang, G. (2015) Silicon isotopic chemistry in the C hangjiang E stuary and coastal regions: Impacts of physical and biogeochemical processes on the transport of riverine dissolved silica. Journal of Geophysical Research: Oceans 120, 6943-6957.

Zhang, Z., Sun, X., Dai, M., Cao, Z., Fontorbe, G. and Conley, D.J. (2020) Impact of human disturbance on the biogeochemical silicon cycle in a coastal sea revealed by silicon isotopes. Limnology and Oceanography 65, 515-528.

Table1

LAVO Lake	Total Watershed Area (km^2)	Drainage Ratio	Inflow	Outflow	Dominant Watershed Lithology	Estimated Curve Number	Lake Surface Area (km^2)	Shoreline Length (km)	Shore Development	Lake Volume ($x10^5$ m^3)	Average Depth (m)	Maximum Depth (m)	Hydraulic Retention Time (HRT; years)
Manzanita	29.5	164	Upper Manzanita Creek, Little Manzanita Creek[1]	Lower Manzanita Creek[2]	Rhyodacite	63	0.18	2.48	1.65	~1.0	~5.3	~10	0.33
Butte	113.7	135	None observed	Butte Creek[3]	Andesite	58	0.84	11.3	3.8	~60	~7.3	~15	2 - 6[5]
Widow	4.1	34	None observed	Lower Widow Creek[4]	Basalt	33	0.12	1.81	1.48	~5.0	~3.8	~10	--

Table 1: Summary of Manzanita, Butte, and Widow lakes catchment characteristics and morphometry. For closed or semi-closed lakes (BL, WL), size metrics calculated based on GIS data representing full-lake conditions (see Howard and Noble 2018). Curve Number is an empirical parameter that predicts the likelihood of overland runoff for a rainfall event; Shoreline Development is shoreline length relative to a circle of the same area

[1]Small ephemeral stream; a dry stream bed indicated a potential inflow, but no flow was observed during the 2012-2014 sampling period

[2]Lower Manzanita Creek sampled by USGS 1979-1981, data accessed via NWIS portal, site number: 11376038

[3]Outflow in Butte Creek was observed May-September in 2012. In 2013/2014, Butte Lake level dropped below the outflow level and outflow ceased.

[4]Although a dry creek/stream bed indicated a possible inflow path; no flow was observed during sampling activities 2012-2014.

[5]See discussion in Howard and Noble (2018)

Table2 Click here to access/download;Table;Table 2.pdf

	Date	Sample location	Dissolved Si concentration (mg/L)	Chlorophyll-a concentrations (µg/L)	Secchi depth (m)	$\delta^{30}Si_{dSi}$ (‰ vs. NBS28)	$\delta^{30}Si_{bSi}$ (‰ vs. NBS28)
Butte Lake	2012-08-08	0 m	--	1.1	5.9	--	-1.02
		4 m	--	3.4		--	--
		9 m	--	4.8		--	--
	2013-08-09	0 m	3.6	4.3	5.5	--	--
		7.5 m	4.5	21		--	--
		10.5 m	4.4	18.2		--	--
	2014-05-31	0 m	2.4	4.1	5	1.55	-0.74
		6 m	2.6	4.9		1.34	--
		10 m	3.2	18.8		1.15	--
	2014-08-06	0 m	2.7	8.4	< 3*	1.63	--
		7 m	3.9	80.4		1.3	--
		9 m	4.2	17		1.57	--
	2014-09-27	0 m	3	16.9	3	1.27	--
		9.5 m	2.8	--		1.21	--
	Range		2.1	79.3		0.48	
	Mean		3.4	15.6		1.38	
	SD		0.8	20.7		0.18	
Manzanita Lake	2014-05-29	Inflow (UMC)	16			1.01	-0.4
	2014-09-26		18			1.01	-0.81
	2014-05-29		12			1.94	0.27
	2014-09-26	Outflow (LMC)	12	--		--	--
	2014-09-29		--	--		1.78	--
	2012-06-24	0 m	--	0.31	7.75	--	--
		4 m	--	0.48		--	--
		7 m	--	0.6		--	--
	2012-08-12	0 m	--	0.71	7	--	-0.96
		4.5 m	--	1.3		--	--
		7.5 m	--	0.98		--	--
	2012-09-29	0 m	--	0.37	9.7	--	--
		4 m	--	2.2		--	--
		9 m	--	0.49		--	--
	2013-08-13	0 m	11	2.07	7.5	--	-1.59
		3.5 m	14	4.41		--	--
		8 m	13	2.66		--	--
	2014-06-01	0 m	13	0.58	9.3	2.1	-1.3
		4 m	12	1.18		1.29	--
		8 m	13	2.26		1.37	--
	2014-08-16	0 m	12	2.98	--	1.71	--
		5 m	14	5.01		1.43	--
		8 m	14	6.04		1.56	--
	2014-09-29	0 m	12	7.4	6.5	2.79	-1.11
		7 m	14	1.7		1.42	--
	Range ML		3	5.73		1.5	
	Mean ML		13	2.19		1.71	
	SD ML		1	2.04		0.51	
Widow Lake	2012-06-21	0 m	--	1.28	7.75	--	--
		9 m	--	13.33	--	--	--
	2012-08-10	0 m	--	3.3	7	--	--
	2012-09-29	0 m	--	5	8	--	--
		9 m	--	5.37	--	--	--
	2013-08-10	0 m	3	22.78	5	--	--
		9 m	2.8	42.07	--	--	--
	2014-05-31	0 m	2.4	6.76	8	0.94	--
	2014-08-15	0 m	2.9	12.29	-	1.5	-0.08
	2014-09-27	0 m	3	36.12	6.5	1.31	--
	Range		0.6	40.79			
	Mean		2.8	17.19			
	SD		0.2	14.28			

Table3

Group 1 ($\delta^{30}Si_{bSi}$ > -0.14 ‰)		Group 2 (-0.21 < $\delta^{30}Si_{bSi}$ < -0.51 ‰)[1]		Group 3 (-0.55 < $\delta^{30}Si_{bSi}$ < -0.66 ‰)		Group 4 (-0.69 < $\delta^{30}Si_{bSi}$ < -1.1 ‰)		Group 5 ($\delta^{30}Si_{bSi}$ < -1.1 ‰)	
Taxa	**IV**	**Taxa**	**IV**	**Taxa**	**IV**	**Taxa**	**IV**	**Taxa**	**IV**
Tabellaria flocculosa	79	*Stephanodiscus spp 3*	21	*Karayevia clevei*	73	*Reimeria sinuata*	45	*Fragilaria crotonensis*	73
Navicula spp 1	63	*Distrionella incognita*	20	*Pseudostaurosira parasitica*	56	*S. construens var venter*	42	*Fragilaria mesolepta*	60
Discostella stelligera	56	*Fragilaria grunowii*	18	*Staurosirella pinnata*	52	*Diatoma mesodon*	42		
Nitzschia perminuta	55	*Fragilaria perdelicatissima*	15	*Pseudostaurosira confusa*	50	*Stephanodiscus spp 2*	40		
Encyonopsis spp 1	54	*Fragilaria tenuissima*	15	*Nitzschia liebertruthii*	50	*Pseudostaurosira brevistriata*	36		
Encyonopsis spp 5	52			*P. pseudoconstruens*	49				
Navicula spp 2	51			*Planothidium haynaldii*	47				
Encyonopsis spp 4	51			*Achnanthidium exiguum*	46				
Lindavia spp	46			*Pseudostauosiropsis spp*	45				
Stauroneis neohyalina	44			*Geisleria spp*	44				
Encyonema lange-bertalotii	41			*Navicula spp*	38				
Stauroneis phoenicenturon	41								
Gomphonema acuminatum	40								
Encyonopsis spp 3	37								
Gomphonema brebissonii	36								
Pinnularia spp 3	35								

Significant ($\alpha < 0.05$) indicator taxa for Groups 1, 3, 4, 5 (Groups based on groupings determined from $\delta^{30}Si_{bSi}$ values). IV = indicator value

[1]Although not significant, top taxa for Group 2 are also given.

Figure1

Click here to access/download;Figure;Figure 1.pdf

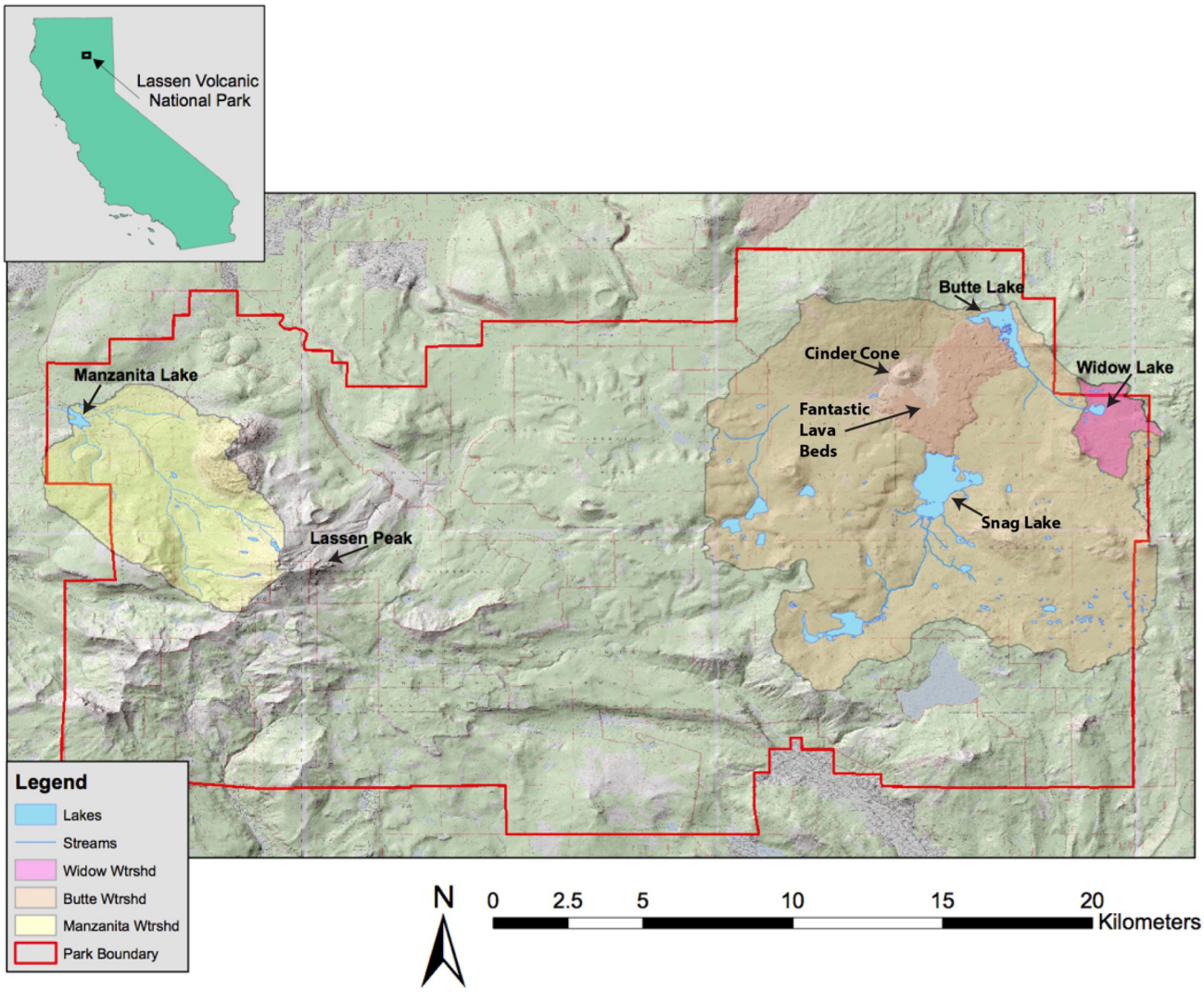

Figure2

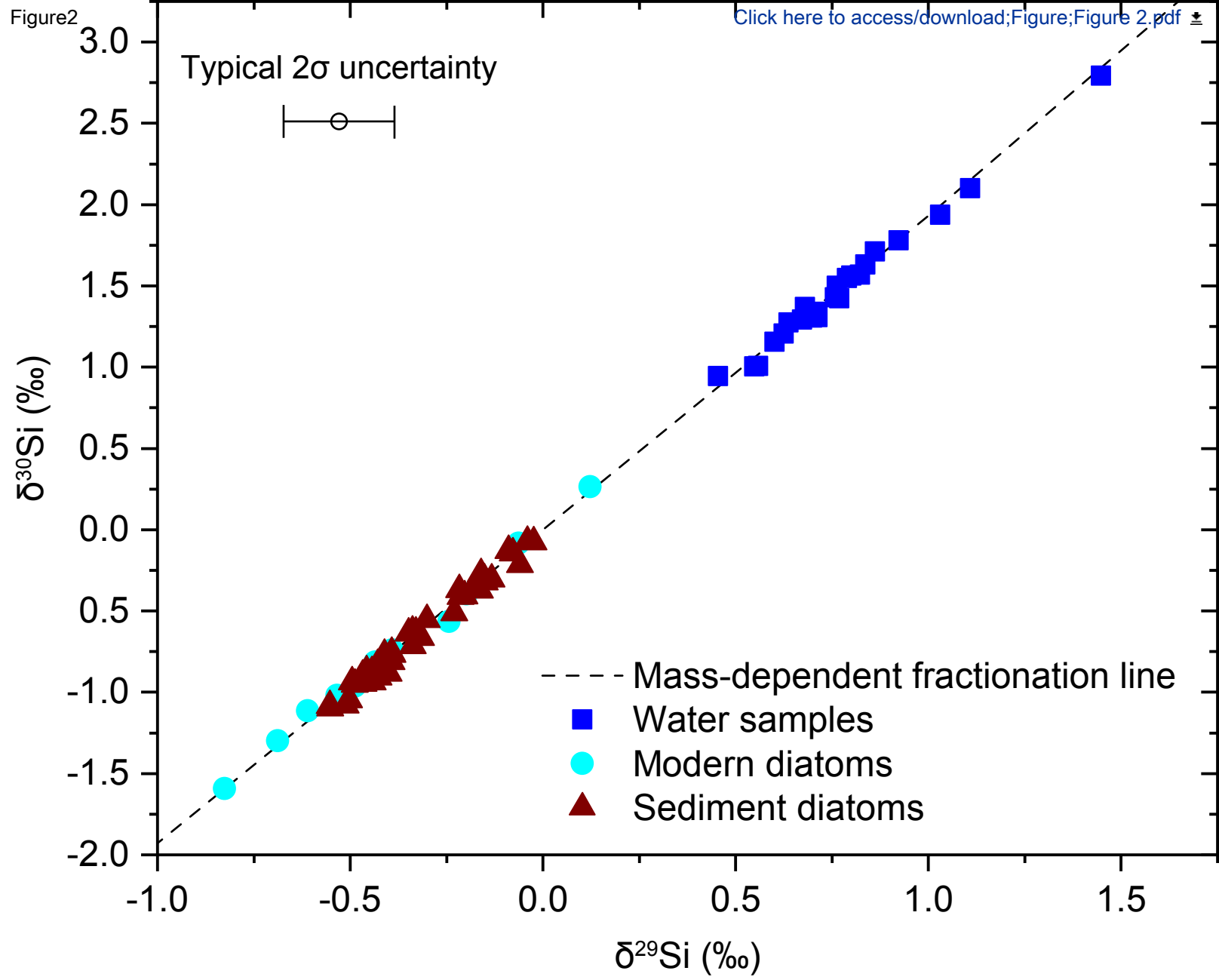

Figure3

Click here to access/download;Figure;Figure 3.pdf

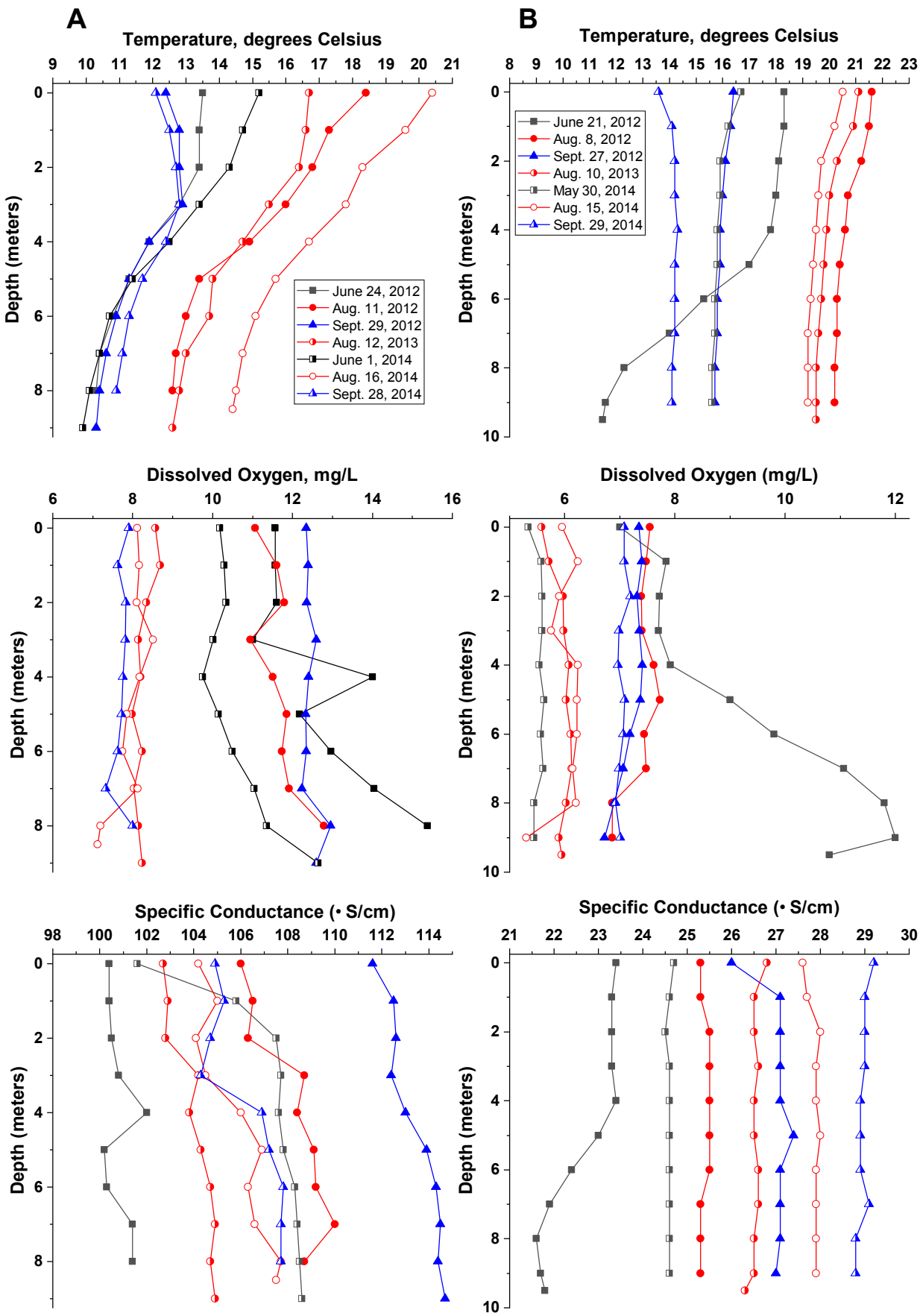

Figure4

Click here to access/download;Figure;Figure 4.pdf

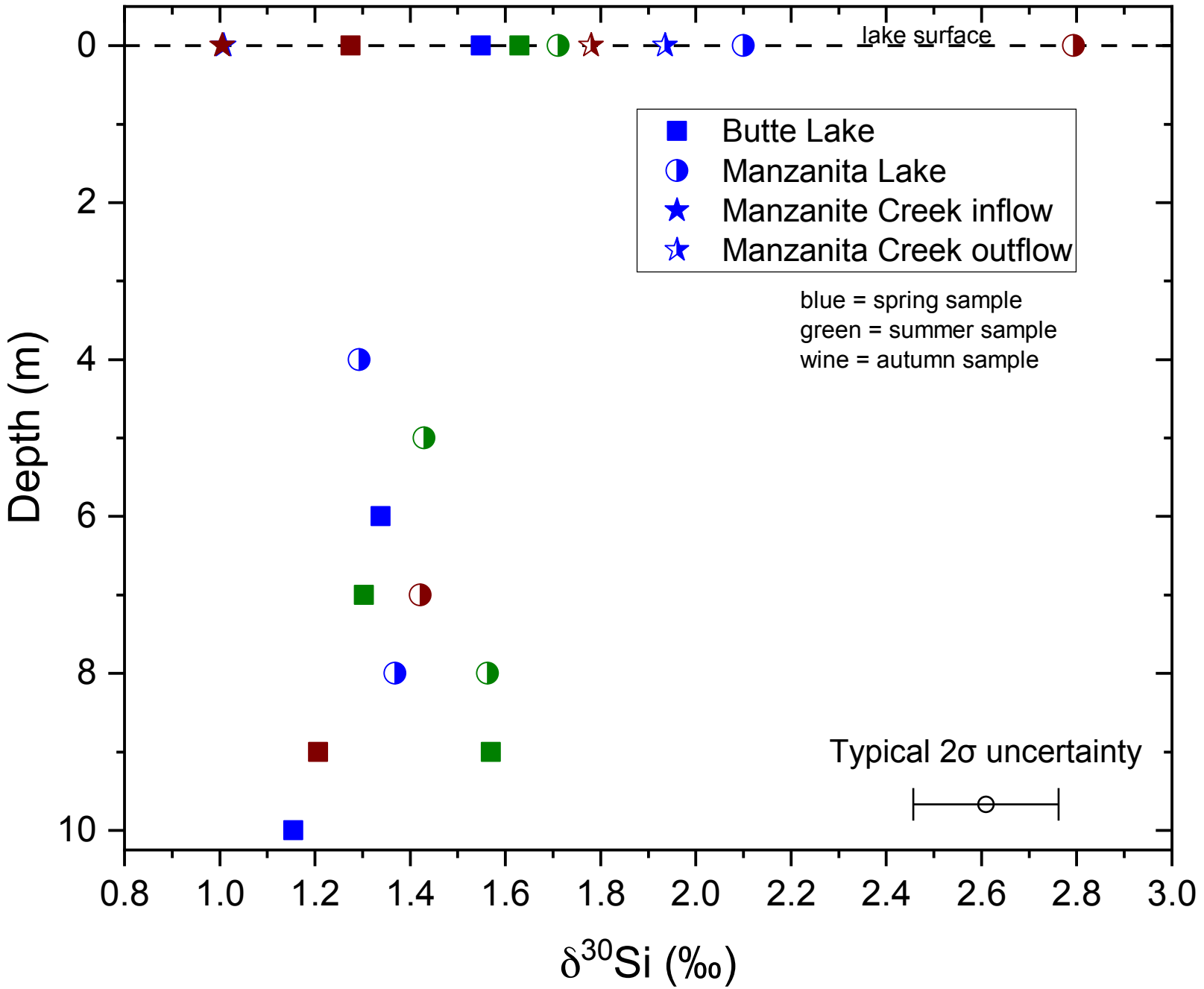

Figure5

Click here to access/download;Figure;Figure 5.pdf

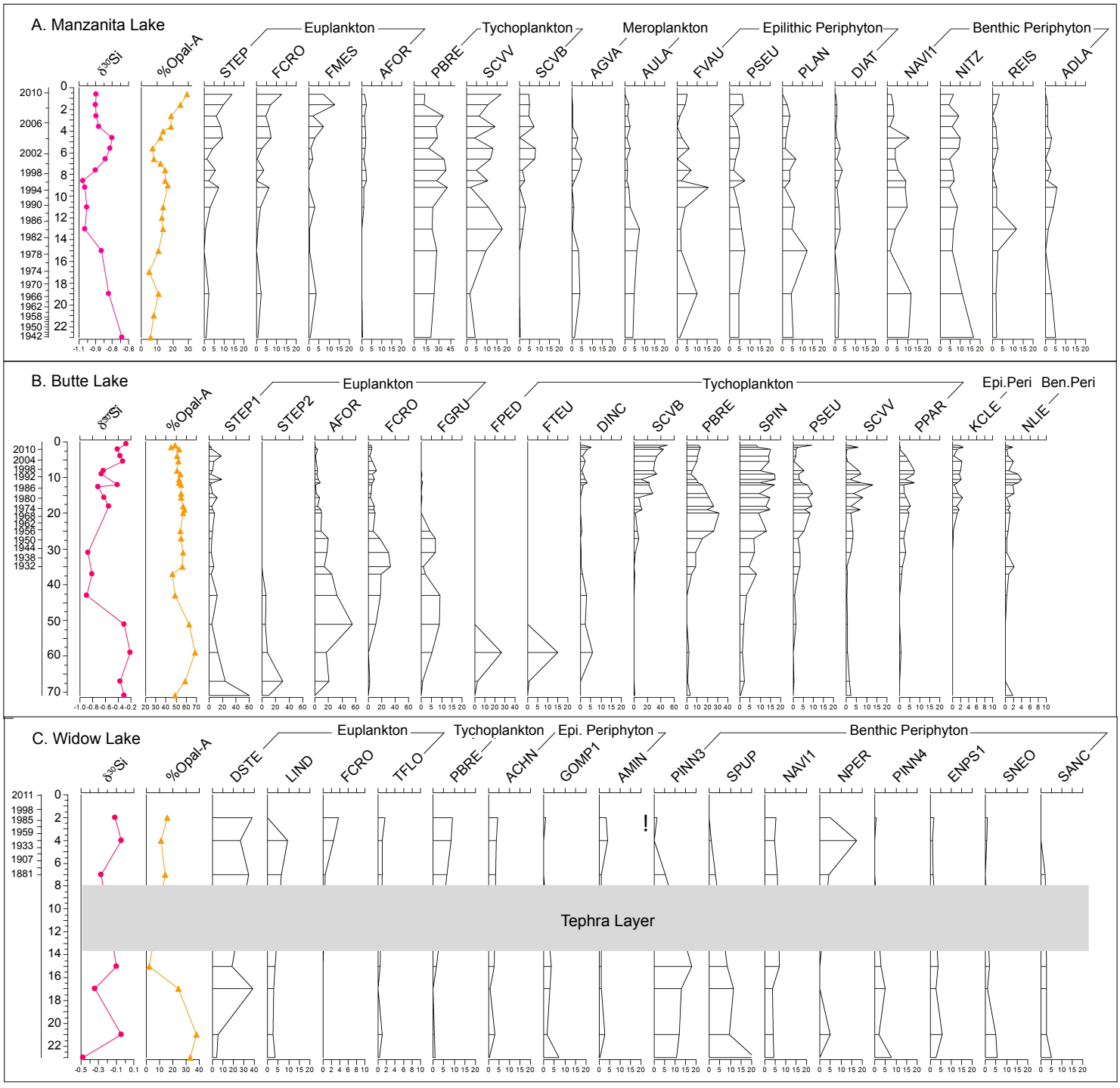

Figure6

Click here to access/download;Figure;Figure 6.pdf

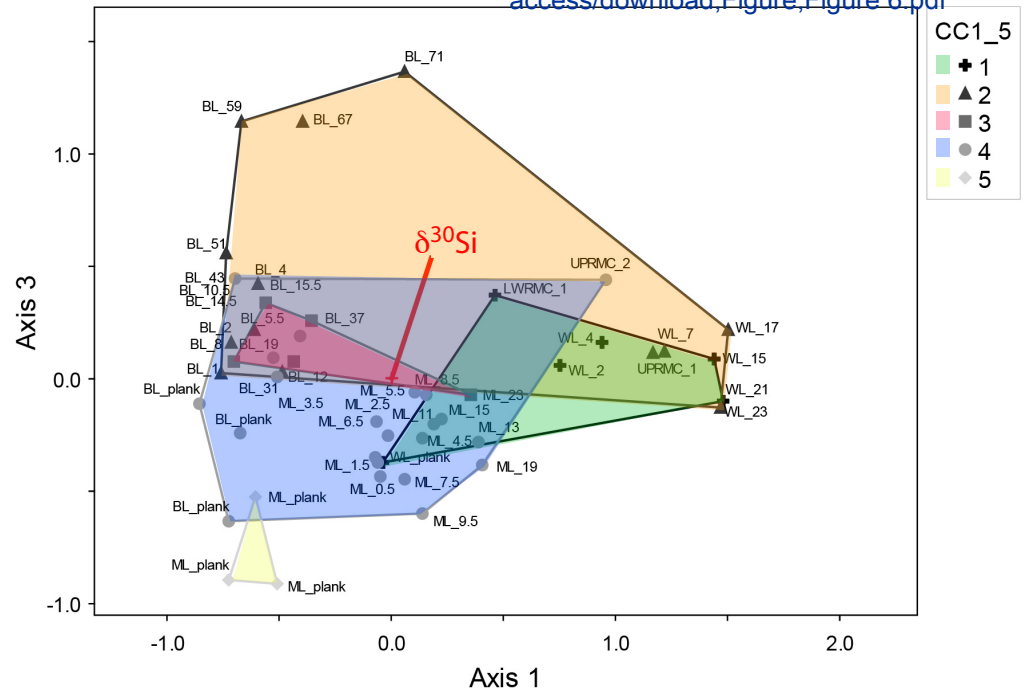

Figure7

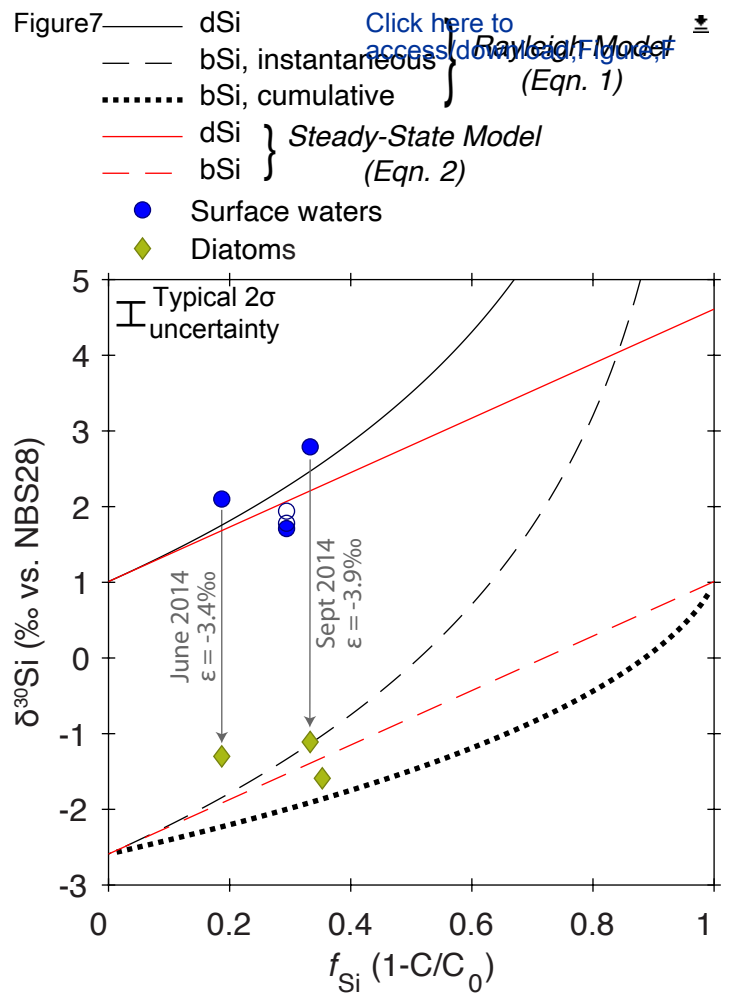

Figure8

Click here to access/download;Figure;Figure 8.pdf

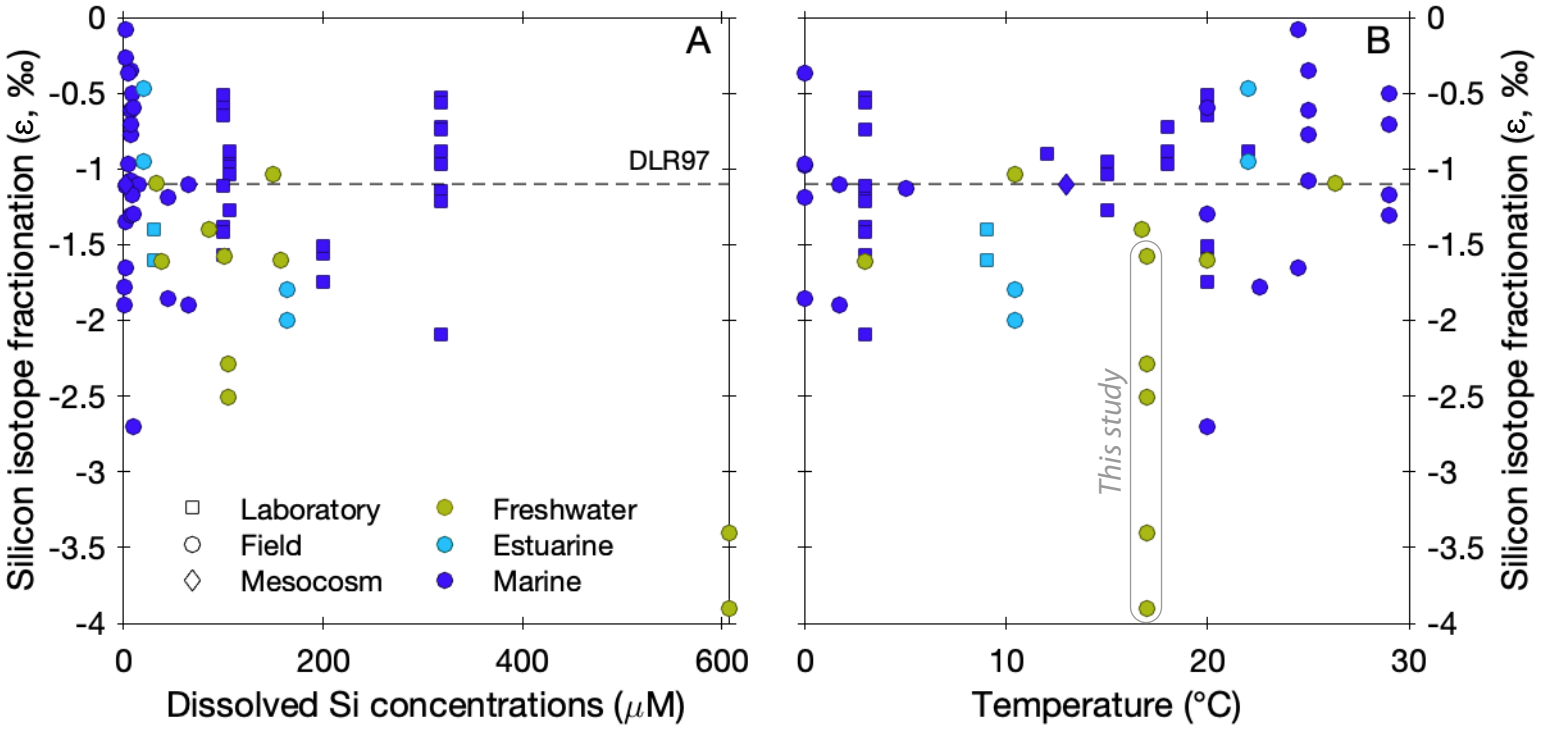

Figure9